

# The *Herschel*\* Virgo Cluster Survey

## XX. Dust and gas in the foreground Galactic cirrus

S. Bianchi<sup>1</sup>, C. Giovanardi<sup>1</sup>, M. W. L. Smith<sup>2</sup>, J. Fritz<sup>3</sup>, J. I. Davies<sup>2</sup>, M. P. Haynes<sup>4</sup>, R. Giovanelli<sup>4</sup>, M. Baes<sup>5</sup>, M. Bocchio<sup>6</sup>, S. Boissier<sup>7</sup>, M. Boquien<sup>8</sup>, A. Boselli<sup>7</sup>, V. Casasola<sup>1</sup>, C. J. R. Clark<sup>2</sup>, I. De Looze<sup>9</sup>, S. di Serego Alighieri<sup>1</sup>, M. Grossi<sup>10</sup>, A. P. Jones<sup>6</sup>, T. M. Hughes<sup>11</sup>, L. K. Hunt<sup>1</sup>, S. Madden<sup>12</sup>, L. Magrini<sup>1</sup>, C. Pappalardo<sup>13, 14</sup>, N. Ysard<sup>6</sup>, S. Zibetti<sup>1</sup>

<sup>1</sup> INAF–Osservatorio Astrofisico di Arcetri, Largo E. Fermi, 5, I-50125 Firenze, Italy. e-mail: sbianchi@arcetri.astro.it

<sup>2</sup> School of Physics and Astronomy, Cardiff University, Queens Building, The Parade, Cardiff, CF24 3AA, UK

<sup>3</sup> Instituto de Radioastronomía y Astrofísica, UNAM, Antigua Carretera a Pátzcuaro #8701, Morelia, Michoacán, Mexico

<sup>4</sup> Cornell Center for Astrophysics and Planetary Science, Space Sciences Bldg., Cornell University, Ithaca, NY 14853

<sup>5</sup> Sterrenkundig Observatorium, Universiteit Gent, Krijgslaan 281-S9, B-9000 Gent, Belgium

<sup>6</sup> Institut d’Astrophysique Spatiale (IAS), UMR 8617, CNRS/Université Paris-Sud, 91405 Orsay, France

<sup>7</sup> Aix Marseille Université, CNRS, LAM (Laboratoire d’Astrophysique de Marseille), UMR 7326, 13388 Marseille, France

<sup>8</sup> Unidad de Astronomía, Facultad de Ciencias Básicas, Universidad de Antofagasta, Avenida Angamos 601, Antofagasta 1270300, Chile

<sup>9</sup> Dept. of Physics & Astronomy, University College London, Gower Street, London WC1E 6BT, UK

<sup>10</sup> Observatório do Valongo, Universidade Federal do Rio de Janeiro, Ladeira Pedro Antônio 43, Rio de Janeiro, Brazil

<sup>11</sup> Instituto de Física y Astronomía, Universidad de Valparaíso, Avda. Gran Bretaña 1111, Valparaíso, Chile

<sup>12</sup> Laboratoire AIM, CEA/DSM - CNRS - Université Paris Diderot, IRFU/Service d’Astrophysique, CEA Saclay, 91191 Gif-sur-Yvette, France

<sup>13</sup> Instituto de Astrofísica e Ciências do Espaço, Universidade de Lisboa, Tapada da Ajuda, 1349-018 Lisboa, Portugal

<sup>14</sup> Observatório Astronómico de Lisboa, Tapada da Ajuda, 1349-018 Lisboa, Portugal

Received ; accepted

### ABSTRACT

We study the correlation between far-infrared/submm dust emission and atomic gas column density in order to derive the properties of the high Galactic latitude, low density, Milky Way cirrus in the foreground of the Virgo cluster of galaxies. Dust emission maps from 60 to 850  $\mu\text{m}$  are obtained from SPIRE observations carried out within the *Herschel* Virgo Cluster Survey, complemented by IRAS-IRIS and *Planck*-HFI maps. Data from the Arecibo legacy Fast ALFA Survey is used to derive atomic gas column densities for two broad velocity components, low and intermediate velocity clouds. Dust emissivities are derived for each gas component and each far-infrared/submm band. For the low velocity clouds, we measure an average emissivity  $\epsilon_v^{\text{LVC}} = (0.79 \pm 0.08) \times 10^{-20}$  MJy  $\text{sr}^{-1} \text{cm}^2$  at 250  $\mu\text{m}$ . After fitting a modified blackbody to the available bands, we estimated a dust absorption cross-section  $\tau_v^{\text{LVC}}/N_{\text{H}_1} = (0.49 \pm 0.13) \times 10^{-25} \text{cm}^2 \text{H}^{-1}$  at 250  $\mu\text{m}$  (with dust temperature  $T = 20.4 \pm 1.5\text{K}$  and spectral index  $\beta = 1.53 \pm 0.17$ ). The results are in excellent agreement with those obtained by *Planck* over a much larger coverage of the high Galactic latitude cirrus (50% of the sky vs 0.2% in our work). For dust associated with intermediate velocity gas, we confirm earlier *Planck* results and find a higher temperature and lower emissivity and cross-section. After subtracting the modelled components, we find regions at scales smaller than 20' where the residuals deviate significantly from the average, cosmic-infrared-background dominated, scatter. These large residuals are most likely due to local variations in the cirrus dust properties (and/or the dust/atomic-gas correlation) or to high-latitude molecular clouds with average  $N_{\text{H}_2} \lesssim 10^{20} \text{cm}^{-2}$ . We find no conclusive evidence for intracluster dust emission in Virgo.

**Key words.** dust, extinction - radiation mechanisms: thermal - infrared, submillimeter, radio lines: ISM - local interstellar matter

### 1. Introduction

Diffuse far-infrared (FIR) emission from high-Galactic latitude dust (the Milky Way *cirrus*) is an important test bed for models of interstellar grains. The thinness of the Galactic disk, our peripheral position in it, and a viewing direction away from the Galactic plane offer clear advantages to modelling: the main

source of dust heating is provided by the ambient radiation (the Local Interstellar Radiation Field - LISRF; Mathis et al. 1983); the diffuse radiation gradients perpendicular to the disk being small (as shown by radiative transfer models of galactic disks; Bianchi et al. 2000; Bocchio et al. 2013; Popescu & Tuffs 2013); thus the mixing of dust at different temperatures (and/or with different properties) along a single line of sight is limited.

Starting from the first detection of the cirrus emission by the IRAS satellite (Low et al. 1984), a tight correlation of the FIR surface brightness with the atomic gas column density was ob-

\* *Herschel* is an ESA space observatory with science instruments provided by European-led Principal Investigator consortia and with important participation from NASA.

served (Boulanger & Perault 1988). The cirrus surface brightness per H I column density (a quantity known as *emissivity*) measured in the 60 and 100  $\mu\text{m}$  IRAS bands was then used to verify the predictions or constrain the properties of early interstellar grain models (Draine & Lee 1984; Désert et al. 1990).

With the advent of the instruments aboard the COBE satellite, and in particular the FIRAS spectrophotometer, it was possible to study the Spectral Energy Distribution (SED) of the cirrus up to the peak of thermal emission and beyond. Boulanger et al. (1996) found a tight correlation with H I column density and measured the emissivity up to 1 mm. After fitting a modified blackbody (MBB) to the data, the dust absorption cross-section per unit H I column density was retrieved, which was found to be in agreement with the available dust models. Since then, the FIRAS emissivity has been one of the major constraints to dust models, which were formulated to reproduce its SED levels and shape, resulting in an average dust cross-section  $\propto \nu^\beta$ , with  $\beta \approx 1.8 - 2$  (see, e.g., Draine 2003; Zubko et al. 2004; Compiègne et al. 2011; Jones et al. 2013).

The recent analysis of data from the *Planck* satellite, however, revealed an inconsistency between *Planck* and FIRAS, which prompted a recalibration on planet fluxes of the 350 and 550  $\mu\text{m}$  data from the High Frequency Instrument (HFI; Planck Collaboration VIII 2014). As a result, the newly determined emissivities have been found to be lower than the FIRAS values, and with a reduced dust cross-section spectral index ( $\beta \approx 1.6$ ; Planck Collaboration XI 2014; Planck Collaboration Int. XVII 2014). These results suggest that a re-evaluation of the dust model parameters may be required, and in particular of the grain size distributions and relative contribution of grains of different chemical composition to the SED at  $100 \mu\text{m} \lesssim \lambda \lesssim 1 \text{ mm}$ . Furthermore, the higher resolution of *Planck* data with respect to FIRAS highlighted local dust emissivity variations with the environment (Planck Collaboration XI 2014; Planck Collaboration Int. XVII 2014).

A tenuous cirrus is seen in the foreground of the Virgo cluster of galaxies ( $l = 283.8^\circ$ ,  $b = 74.4^\circ$ ) through scattered starlight in deep optical (Rudick et al. 2010; Mihos 2015) and UV images (Cortese et al. 2010; Boissier et al. 2015); it corresponds to low extinction, with  $0.02 < E(B - V) < 0.1$  (Boissier et al. 2015). Its emission is clearly detected at 250, 350 and 500  $\mu\text{m}$  in images obtained by the SPIRE instrument (Griffin et al. 2010) aboard the *Herschel* Space Observatory (Pilbratt et al. 2010), as part of the *Herschel* Virgo Cluster Survey (HeViCS; Davies et al. 2010a, 2012; Auld et al. 2013). In this work, we will derive the dust emissivity of the HeViCS cirrus in the SPIRE bands. This will allow to verify the latest *Planck* results, since the SPIRE calibration also is based on planet models. Besides, the 250  $\mu\text{m}$  band will fill the gap between the IRAS and *Planck* data, and complement the lower sensitivity and resolution COBE-DIRBE emissivity at 240  $\mu\text{m}$  (Planck Collaboration Int. XVII 2014). When compared to the *Planck* large area estimates, the relatively small sky coverage of the HeViCS field will also highlight local emissivity variations.

The emissivities will be derived using H I observations from the Arecibo Legacy Fast ALFA survey (hereafter ALFALFA Giovanelli et al. 2005). The high resolution of the ALFALFA data (FWHM=3'5) is comparable to that of the longest wavelength data dominated by dust thermal emission (the 850  $\mu\text{m}$  *Planck*-HFI band, with 4'8); it is also a factor two better than other H I data used to derive dust emissivities: previous large-area studies (Boulanger et al. 1996; Planck Collaboration XI 2014) used ob-

servations at FWHM=0.6° from the Leiden/Argentine/Bonn (LAB) Survey of Galactic H I (Kalberla et al. 2005). The FWHM=14'5 GASS H I survey of the southern sky has been used in Planck Collaboration Int. XVII (2014), while Planck Collaboration XXIV (2011) exploited Green Bank Telescope maps at FWHM=9'1. Only in the recent work of Reach et al. (2015) Arecibo telescope data from the Galactic ALFA (GALFA; Peek et al. 2011) survey have been used to study the correlation between H I column density of isolated high-latitude clouds and *Planck*-based dust column densities.

The resolution of the ALFALFA survey thus allows a characterization of the residuals to the dust-H I correlation at smaller scales. In fact, one of the aims of HeViCS is the detection of dust emission from the intracluster medium (ICM), once the structure of the foreground cirrus is subtracted using Galactic H I as a template. The presence of the cirrus is indeed the limiting factor in these studies: so-far the only claim of the detection of FIR emission from the ICM is that on the Coma cluster by Stickel et al. (1998), using data from the ISOPHOT instrument aboard the ISO satellite. However, the analysis of five other clusters with analogous data and techniques yielded no detection (Stickel et al. 2002); a following analysis of Coma using data from the *Spitzer* satellite dismissed the putative emission as cirrus contamination (Kitayama et al. 2009).

This paper is organised as follows: in Sect. 2 we present the ALFALFA and HeViCS data, together with other ancillary maps used in this work. In Sect. 3 we describe the method used to derive the correlation between dust and H I. The fitted emissivities are presented in Sect. 4, while Sect. 5 is dedicated to the derivation of the mean opacity cross section from the emissivity SEDs. The possible Galactic origin of the largest residuals is discussed in Sect. 6, while in Sect. 7 we put constraints on the dust emission from the Virgo ICM. The work is summarised in Sect. 8.

## 2. Data sets

The HeViCS project obtained FIR/submm images of about 84 deg<sup>2</sup> over the Virgo cluster, using the photometers aboard *Herschel*. The survey area was covered with four overlapping fields. The survey strategy and observations are described in detail in several previous publication of the HeViCS series (e.g. Davies et al. 2010a, 2012; Auld et al. 2013).

In this section we describe the H I and FIR/submm data sets we have used to derive the emissivity of MW dust in the HeViCS footprint.

### 2.1. H I ALFALFA Data

ALFALFA (Giovanelli et al. 2005) is a spectro-photometric, wide-field survey at the Arecibo radiotelescope aimed to delivering the properties of galaxies in the local Universe, as revealed by the 21 cm line of interstellar atomic Hydrogen. It covers a spectral range of 100 MHz with a resolution of 25 KHz (~5.1 km/s), including the spectral domain of interstellar and perigalactic emission. It covers uniformly the sky footprint of the HeViCS survey, with an angular resolution of 3.5' FWHM. Data have been taken in drift mode, i.e. with the telescope scanning tracks of constant declination at the sidereal rate. Two independent polarization components of the data are recorded. Basic data units are three-dimensional. Each data cube is complemented by a two-dimensional map of the continuum background and a 3-d array carrying the data quality of each pixel.

The use of the ALFALFA data for this work requires two important differences in the generation of the data cubes, with

respect to the pipeline processing adopted for extragalactic applications: (i) the spectral stretch of the data cubes is restricted to the range between  $-1000$  and  $+1050$  km/s, which included 400 spectral channels spaced by 25 KHz (5.1 km/s) and (ii) the flux scale is calibrated in Kelvin degrees of antenna temperature  $T_A$ . The sky footprint of each cube retains the same size as the standard ALFALFA data cubes, i.e.  $2.4^\circ \times 2.4^\circ$ , sampled at  $1'$  pixel separation. The array dimensions of each data cube are then  $400 \times 2 \times 144 \times 144$ , where the '2' refers to the two polarization channels. Each of the four HeViCS fields is fully covered by 10 ALFALFA data cubes, with significant coverage overlap: each point in the HeViCS sky footprint is contained in at least 2 different ALFALFA data cubes.

We then proceeded to the baselining. For each grid and for each polarization, we assembled all the spectra at a given declination in an image, thus obtaining the equivalent of a longslit image. Upon inspection of the central  $1000 \text{ km s}^{-1}$ , and excluding the range occupied by the Galactic line at levels over the noise, we fitted to each spectrum and then removed a polynomial baseline of order up to 6. During this phase we also removed from the "longslit" images any striping due to residual RFI or autocorrelator faults. The processing pipeline was overall satisfactory, except for lines of sight within  $15'$  of the center of galaxy M87, where the strong continuum emission of Virgo A drastically increases noise and associated standing waves makes spectral baselining impossible.

The next phase was the flatfielding of the channel maps. Again separately for the two polarizations, we assembled the grid data for each velocity channel into a different map. These maps were singly inspected and, if required, corrected for residual striping or stepping at the junction between different drifts. The flatfielding procedure was repeated twice: first to eliminate the most obvious defects, and then again for refinement and a double check of the results.

Finally we used an IDL procedure to produce, for each grid, FITS 2D images of the single fully reduced channel maps, or of a velocity range of choice; such a procedure also averages the two polarizations. The swarp software (Bertin et al. 2002) was used to mosaic the FITS output for the grids into maps covering each single HeViCS field and the whole HeViCS footprint. The final maps were converted into units of main beam temperature.

In order to check the H I 21 cm line optical depths in the area, we selected from the NVSS catalog (Condon et al. 1998) all 1400 MHz radiosources with a flux density in excess of 500 mJy located within the HeViCS footprint. This flux limit was computed, given the noise figures of the ALFALFA spectra, to ensure a clear detection ( $S/N > 5$ ) of absorption features from column densities  $N_{\text{HI}} > 5 \times 10^{18} \text{ cm}^{-2}$  with average conditions for spin temperature (100 K) and velocity dispersion ( $5 \text{ km s}^{-1}$ ). We rejected those sources located within  $20'$  of M87, and those not isolated enough or extended, ending up with a list of 22 objects. For each source, the central spectrum was obtained by summing the spectra within a radius of  $3'$ . The emission spectrum was estimated as the median of six similar apertures surrounding in an hexagonal pattern the central source at distance of  $10'$ . The absorption spectrum was derived by subtracting the emission spectrum from the central one, and analysed using standard techniques (see, e.g., Spitzer 1978). Absorption was detected in all 22 spectra, sometimes with multiple features. The optical depths, which we derive with uncertainty of  $\sim 0.003$ , span from 0.01 to 0.4 but with an average of only  $0.058 \pm 0.058$ ; their distribution is illustrated in Fig. 1. The spin temperatures, measured with uncertainty of  $\sim 10$  K, are low, between 50 and 100 K, with only one case exceeding 150 K; their mean value

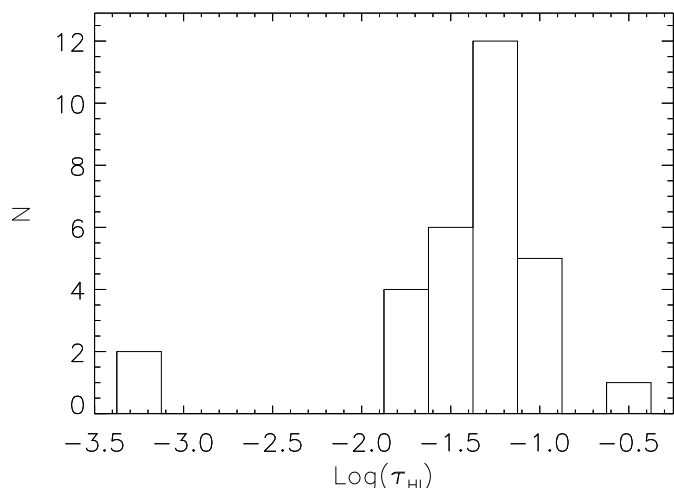


**Fig. 1.** Distribution histogram of the 21 cm line opacity computed for the 30 absorption features detected on the line of sight to NVSS continuum radiosources.

is  $55 \pm 28$  K. The H I column densities range between  $2 \times 10^{18}$  and  $2 \times 10^{20} \text{ cm}^{-2}$ , with a log mean of  $19.60 \pm 0.54$ . Given that the peak brightness temperature of the line is around 3 K, and the noise in the spectra is 0.003K, even taking into account the error in the optical depth corrections, the uncertainty in the total column density is always better than 4%. The average correction factor for optical thickness is  $1.021 \pm 0.029$ ; consequently, throughout the paper, we derived the H I column densities at the optically thin limit.

Planck Collaboration XXIV (2011) has shown that the H I emission can be decomposed into various velocity components by inspecting the channel-to-channel variations of the median and of the standard deviation; the second in particular is more sensitive to structure variation across the field. In Fig. 2 we plot these median and standard deviation spectra for the full HeViCS field. The standard deviation spectrum shows that there are two components, partially overlapping in velocity at  $v_{\text{LSR}} \approx -20 \text{ km s}^{-1}$ . Following the approach of Planck Collaboration XXIV (2011), we thus produced two separate maps of column density using

$$N_{\text{HI}} = 1.823 \times 10^{18} \sum T_b(v) \Delta v \text{ cm}^{-2}$$

with  $T_b$  the main beam temperature spectrum for each pixel. The summation was extended over the velocity range  $-20 \lesssim v_{\text{LSR}} (\text{km s}^{-1}) \lesssim 100$  for Low Velocity Clouds (LVC); over  $-100 \lesssim v_{\text{LSR}} (\text{km s}^{-1}) \lesssim -20$ , for Intermediate Velocity Clouds (IVC). No other significant velocity components are found in the HeViCS field: in particular, there are no conspicuous High Velocity Clouds at the galactic latitude of Virgo (see, e.g., Fig. 1 in Wakker & van Woerden 1997) and indeed the velocity channels in the range  $-200 \lesssim v_{\text{LSR}} (\text{km s}^{-1}) \lesssim -100$  are devoid of large-scale emission features.

We have verified the consistency of the column density values measured on our ALFALFA map with those from the LAB survey (Kalberla et al. 2005). In particular, the Arecibo telescope is known to have significant stray-radiation contamination, which can affect precise determination of the total column densities of large-scale features (see, e.g. Peek et al. 2011). Instead, the LAB data have been corrected for stray radiation. We checked the contamination of the ALFALFA map by smoothing it to the LAB resolution and performing a linear correlation between the column densities of the two dataset, for both the LVC

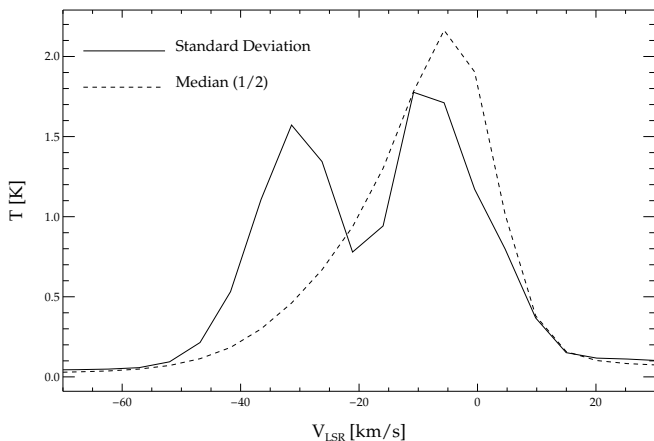


**Fig. 2.** Standard deviation (solid line) and median (dashed line) ALFALFA spectra for the HeViCS field. The median spectrum has been divided by two for ease of presentation

and IVC channels. We found that the ALFALFA map of the LVC channel has a positive offset of  $3.4 \times 10^{19} \text{ cm}^{-2}$  with respect to LAB, and gain close to unity, 1.06. For the IVC channel, the gain is higher (1.16) and the offset smaller ( $1.3 \times 10^{19} \text{ cm}^{-2}$ ). Since in this work we compare our determination of dust emissivities with those obtained using the LAB (Planck Collaboration VIII 2014; Planck Collaboration XI 2014) we corrected our maps for those offsets and gains. We will comment on these corrections in Sect. 4.

## 2.2. HeViCS SPIRE images

Images at 250, 350 and 500  $\mu\text{m}$  were obtained using the SPIRE instrument (Griffin et al. 2010) aboard *Herschel*. The SPIRE data were reduced using the dedicated software HIPE, version 11 (Ott 2010) and following the recommended procedures for maps of extended emission<sup>1</sup>. In previous HeViCS papers we used a custom method for the temperature drift correction and residual baseline subtraction (Bright Galaxy Adaptive Element - BriGAdE; Smith 2012), which is optimised for galaxies. For the larger scale of the cirrus emission, however, BriGAdE tends to flatten the surface brightness gradients. Thus, for the work of this paper we preferred to use the standard *destriper* available within HIPE, adopting a constant offset for each bolometer.

Because of memory limitations and of the relatively small overlap of the four tiles of which the survey is composed, it was not possible to run the *destriper* on the full HeViCS area. In any case, we have preferred to conduct our analysis on the individual fields, to study possible variations of the dust properties across the survey area. This also minimizes the impact of larger scale gradients resulting from diffuse Galactic emission and zodiacal light, which are poorly sampled by our limited-size tiles. As SPIRE is only sensitive to relative field variations, each field is offset from the others because of their different median surface brightness levels. While it is possible to set an absolute flux offset by correlating *Herschel* and *Planck* observations within HIPE, we retained the original levels and relied on our own determination of the zero levels with respect to H I column density (see Sect. 3).

<sup>1</sup> For information on the adopted calibration, beam sizes and color corrections, see the SPIRE Handbook v.2.5 (2014), available at the *Herschel* Astronomer's website.

Images were created in Jy/beam with pixel sizes of 6, 8 and 12" at 250, 350 and 500  $\mu\text{m}$ . These values are about 1/3 of the main beam FWHM, which, for the adopted pixel sizes, is about 18, 24.5 and 36". Units were finally converted to  $\text{MJy sr}^{-1}$ . The calibration uncertainty is 7% at all SPIRE wavelengths, including uncertainties in the model, in the measurements of the calibrator flux, and in the estimate of the beam areas.

We did not use the PACS (Poglitsch et al. 2010) data taken in parallel with SPIRE. The cirrus is indeed detected at very faint levels at 160  $\mu\text{m}$ , but the images contain large scale artifacts of the data reduction process that prevented their usage.

## 2.3. IRAS & Planck

We used 60 and 100  $\mu\text{m}$  maps from the IRAS satellite (Neugebauer et al. 1984). Images in  $\text{MJy sr}^{-1}$  with pixels size 1/5 were obtained using the dataset and procedures from the *Improved Reprocessing of the IRAS Survey* (IRIS; Miville-Deschênes & Lagache 2005). The PSF of the IRIS maps is estimated to be Gaussian with FWHM= 4/0 and 4/3 at 60 and 100  $\mu\text{m}$ , respectively. At both wavelengths, calibration uncertainties amount to about 15% and results from the uncertainties in the gain and color correction with respect to data from the poorer-resolution, better-photometric accuracy DIRBE instrument on the COBE satellite, which was used to recalibrate the IRAS data.

Maps at 350, 550 and 850  $\mu\text{m}$  (857, 545 and 353 GHz, respectively) produced by the High Frequency Instrument (HFI) aboard the *Planck* satellite were taken from the 2013 data release (Planck Collaboration I 2014). These channels are dominated by foreground dust emission; the 850  $\mu\text{m}$  map allows us to extend the analysis to longer wavelengths than those covered by SPIRE, while the maps at 350 and 550  $\mu\text{m}$  provide a consistency check between SPIRE and HFI (and in general, a sanity check with the analysis in Planck Collaboration XXIV 2011 and Planck Collaboration XI 2014). We have used the data corrected for Zodiacal emission, and regridded them from the original HEALpix format to a RA/Dec frame centered on the HeViCS field.

While maps at 350 and 550  $\mu\text{m}$  are already provided in  $\text{MJy sr}^{-1}$ , the map at 850  $\mu\text{m}$  was converted into those units by multiplying it by the band-average unit conversion coefficient as described in Planck Collaboration IX (2014). The map at 850  $\mu\text{m}$  was found to be significantly contaminated by the Cosmic Microwave Background (CMB). A few *Planck*-based models of the CMB are available, obtained with different methods (Planck Collaboration XII 2014). We first used the CMB model produced with the leading method, SMICA, which was found successful in subtracting the CMB contamination from maps of M31 (Planck Collaboration Int. XXV 2015). However, in the SMICA map the CMB fluctuations are not defined in an aperture of  $1^\circ$  around M87; large residuals are left in the area after the subtraction, which affect the derivation of the 850  $\mu\text{m}$  emissivity in field V2. Thus, we preferred the NILC model, which shows CMB features also close to M87. For the CMB subtraction (and emissivity analysis) in the other HeViCS fields, the use of the NILC map produces equivalent results to SMICA.

The PSF of *Planck* images can be described by Gaussians with FWHM very similar to those of IRAS: 4/3, 4/7 and 4/8 at 350, 550 and 850  $\mu\text{m}$ , respectively (Planck Collaboration I 2014). Calibration uncertainties are of 1% for the CMB calibrated 850  $\mu\text{m}$  maps, and 10% for the two shorter wavelengths maps, whose calibration is based on planets: in the latter case the calibration uncertainty is not completely uncorre-

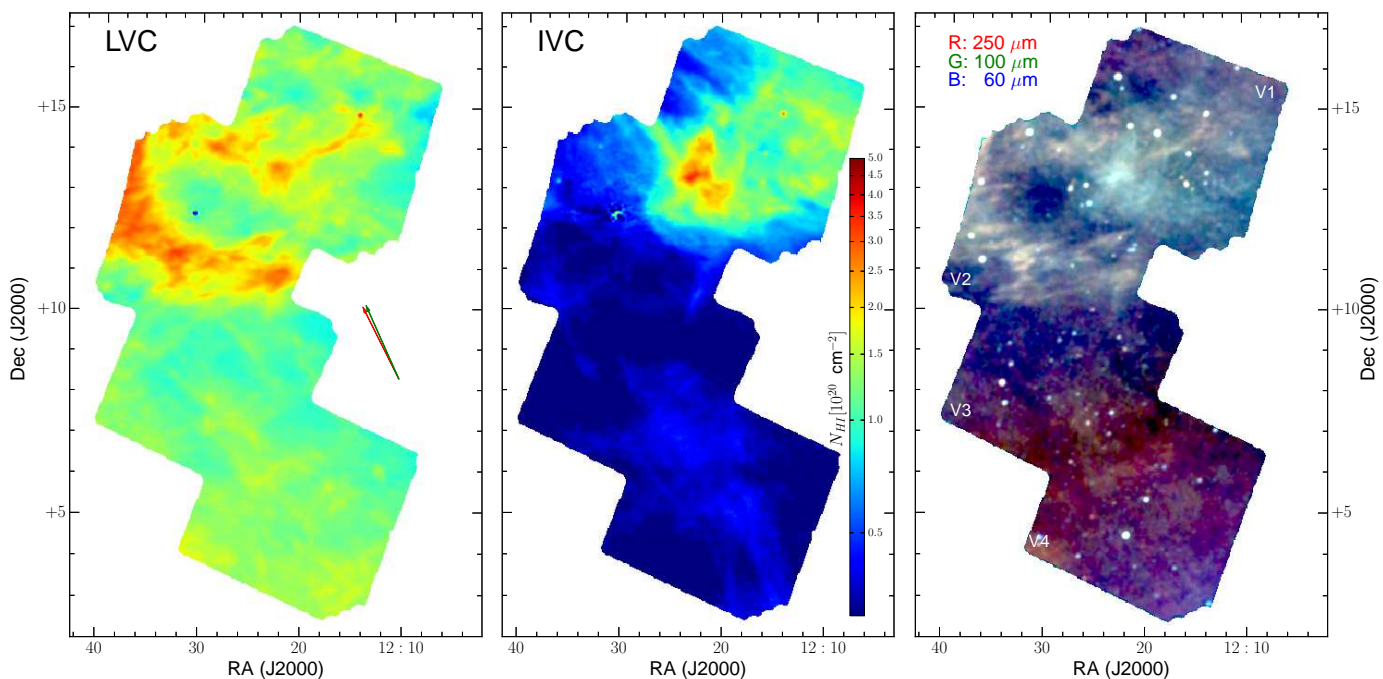


**Fig. 3.** The HeViCS field: ALFALFA H I column density of the LVC component with  $-20 < v_{\text{LSR}}/\text{km s}^{-1} < 100$  (left panel); and of the IVC component with  $-100 < v_{\text{LSR}}/\text{km s}^{-1} < -20$  (central panel). Both components are shown with the same color scale. The RGB composite in the right panel shows dust emission at  $60\ \mu\text{m}$  (blue),  $100\ \mu\text{m}$  (green) and  $250\ \mu\text{m}$  (red). All images are convolved to a resolution of  $\text{FWHM}=4.8$ . For this figure, the full  $250\ \mu\text{m}$  map was obtained by removing the mutual offsets between the HeViCS fields; the quantitative analysis is instead done separately on each of the four fields, as motivated in Sect. 2.2. In the left panel, the red and green arrows indicate the direction of the Galactic and ecliptic North, respectively.

lated to that of SPIRE, both sharing a 5% uncertainty in the model flux of one of the HFI’s calibrators, the planet Neptune (Planck Collaboration VIII 2014).

#### 2.4. Convolved and regridded maps

For each of the HeViCS fields (named V1, V2, V3 and V4 from North to South) we have regridded all data sets to a common J2000 RA & Dec frame in gnomonic projection, with pixels size  $1/5$ . All maps were convolved to the poorer resolution of *Planck*  $850\ \mu\text{m}$  ( $4.8$ ) using simple Gaussian kernels. Excluding border regions with incomplete PSF sampling, the total area analysed amounts to  $76\ \text{deg}^2$  ( $64\ \text{deg}^2$  when excluding the masked sources). In Fig. 3 we show the gas column density of the LVC component (left panel), the IVC component (central panel) and an RGB representation of dust emission (right panel) of the full HeViCS area.

The left panel of Fig. 3 shows that LVC gas is present in all the HeViCS tiles. It is more diffuse in the southernmost fields V3 and V4, with an average column density  $N_{\text{H I}} = 1.2 \times 10^{20}\ \text{cm}^{-2}$ . Most of the gas is in the ring-like structure of field V2, coincidentally centered on the center of the Virgo cluster, where the peak column density is  $3.3 \times 10^{20}\ \text{cm}^{-2}$ . A long filament is the main structure in the center of field V1<sup>2</sup>.

Most of the IVC component (central panel) is instead concentrated in field V1 and V2, with a peak column density  $N_{\text{H I}} = 3.5 \times 10^{20}\ \text{cm}^{-2}$  in the overlap of the two tiles. This region corre-

sponds to a column density enhancement at the border of a loose cloud known as *clump S1*, part of a larger Galactic structure named *Intermediate-Velocity (IV) Spur* (Kuntz & Danly 1996). The analysis of interstellar absorption lines towards the direction of the IV-Spur has shown that this gas resides at large distance from the Galactic plane, with a distance bracket between  $0.3$  and  $2.1\ \text{kpc}$  (Kuntz & Danly 1996; Wakker 2001). Because of this structure, the average column density of the IVC component in field V1 is comparable to that of LVC ( $N_{\text{H I}} = 1.1 \times 10^{20}$  vs  $1.4 \times 10^{20}\ \text{cm}^{-2}$ , respectively). Fields V3 and V4 have instead a tenuous IVC component, with an average column density  $N_{\text{H I}} = 3.2 \times 10^{19}\ \text{cm}^{-2}$ . Also, in these fields IVC and LVC show a larger overlap in velocity space, and our simple  $v_{\text{LSR}}$  cut cannot provide a clear separation of the two components.

The RGB map in the right panel of Fig. 3 shows the overall correlation between dust and atomic gas: in particular, the ring-like feature of field V2 is also visible in dust emission (as it is in UV scattered light; Boissier et al. 2015). Also, dust emission associated to IVC gas appears to be bluer than that coming from LVC gas. The correlation is evident also in fields V3 and V4, where dust emission is tenuous.

### 3. Analysis

Our analysis follows the approach of Planck Collaboration XXIV (2011). The surface brightness map of dust emission at frequency  $\nu$ ,  $I_\nu$ , can be written as:

$$I_\nu = \epsilon_\nu^{\text{LVC}} \times N_{\text{H I}}^{\text{LVC}} + \epsilon_\nu^{\text{IVC}} \times N_{\text{H I}}^{\text{IVC}} + O_\nu + E_\nu \times (b - b_0) + R_\nu, \quad (1)$$

where  $N_{\text{H I}}^{\text{LVC}}$  and  $N_{\text{H I}}^{\text{IVC}}$  are the H I column density maps for the low and intermediate velocity cloud components, respectively,  $\epsilon_\nu^{\text{LVC}}$  and  $\epsilon_\nu^{\text{IVC}}$  are the emissivities of dust associated to them. As

<sup>2</sup> The bright point source present in both LVC and IVC maps for field V1 is the Virgo spiral NGC4192 (M98), with Heliocentric radial velocity  $-139\ \text{km s}^{-1}$  and velocity width  $W_{50} = 461\ \text{km s}^{-1}$  (Giovanelli et al. 2007). The artifacts due to M87 are also visible as a lower (higher) than average column density feature in the LVC (IVC) map (see Sect. 2.1).

(most of) the dust emission maps have a relative calibration, the absolute surface brightness levels are unknown: thus, the term  $O_\nu$  is used to describe an offset (or *zero-level*), which will also include any large-scale contribution not directly correlated to the atomic gas. Since SPIRE images are not corrected for zodiacal light (and other data might have residual contribution from this foreground), we also included a term  $E_\nu$  to describe a gradient in ecliptic latitude  $b$  ( $b_0$  being the central latitude in each map). The analysis consists in fitting the first four terms in right-hand side of Eq. 1 to the observed surface brightness  $I_\nu$ . The last term in Eq. 1,  $R_\nu$ , is the map of the residuals, i.e. the difference between the observed and modelled surface brightness.

We neglected in Eq. 1 the contribution of ionized gas, for which there is no available data at a comparable angular scale. Available, larger-scale,  $H\alpha$  surveys (Haffner et al. 2003; Finkbeiner 2003) only show diffuse low-level features in the HeViCS footprint, barely correlated to our H I and dust emission maps. Converting the  $H\alpha$  intensities to ionised gas column densities (as done in Lagache et al. 2000), we estimated that, within each field, the local column density can differ from the field average by up to  $N_{\text{HII}} \approx 3 \times 10^{19} \text{ cm}^{-2}$ . While dust emission associated with the average values would be hidden into  $O_\nu$ , we predicted localised emission to be of the order of the standard deviation of the residuals to our fit (we assumed similar dust properties in the neutral and ionised gas; Lagache et al. 1999, 2000); it is probably smaller, since a significant fraction of high-latitude  $H\alpha$  emission could be due to scattered light rather than to ionised gas (Witt et al. 2010). Thus, dust associated to ionised gas could contribute to the scatter in the  $I_\nu / N_{\text{H}}$  correlation, but it is not likely to produce any large deviation from the assumed model.

The model parameters were estimated using the IDL function `regress` which performs a multiple linear regression fit. Fits were done separately for each of the HeViCS fields. We thus obtain, for each band, four values for each of the parameters,  $\epsilon_\nu^{\text{LVC}}$ ,  $\epsilon_\nu^{\text{IVC}}$ ,  $O_\nu$ ,  $E_\nu$ . We excluded from the fits the regions with significant FIR emission from extragalactic sources, by masking circular apertures of diameter  $4 \times \text{FWHM}$  around the brightest ( $F > 1.1 \text{ Jy}$ ) IRAS point sources (Helou & Walker 1988). The flux limit was selected in order to keep the masked areas to a reasonable size; we will discuss later in Sect. 6 the effect of other unmasked sources on the residuals. Another mask was devised to exclude large deviations from the assumed model: after a first fit was performed to the high signal-to-noise  $250\mu\text{m}$  data, we inspected the probability distribution function (PDF) of  $R_\nu$  and, by fitting a Gaussian to it, estimated the standard deviation of the residuals  $\sigma_R$ . This second mask thus excludes all pixels where residuals at  $250\mu\text{m}$  are  $> 3\sigma_R$ .

Since the fluctuations in residual maps do not behave as white noise, mainly because of the contribution of the Cosmic Infrared Background (CIB), the parameter uncertainties derived from the fit are underestimated (see Planck Collaboration XXIV 2011 for a discussion). Thus, we estimated the uncertainties using a Monte Carlo technique. Simulated images were created starting from a mock map of the residuals, with the same power spectrum of  $R_\nu$ , but with random phase, to which the other terms in Eq. 1 were added, using the observed hydrogen column density maps and the parameters estimated by the fit. The linear regression was repeated on the simulated images, after adding random representations of the instrumental noise to  $I_\nu$  and the two column density maps. The procedure was repeated a thousand times, and a standard deviation retrieved from the resulting PDFs of each of the four parameters. The instrumental noise used in this process was estimated on the convolved and regridded

FIR/submm images by measuring the standard deviation of difference maps: for IRAS, we used the difference between observations of the first and second surveys (HCON-1 and HCON-2, the area was not observed during HCON-3), which were retrieved using the IRIS software; for SPIRE, we used the difference between two maps created combining four scans each; for *Planck*, we took the two *ringhalf* maps provided within the 2013 data release. The error is rather uniform across the HeViCS footprint and amounts to 0.03, 0.05, 0.05, 0.025, 0.015, 0.02, 0.03 and 0.035  $\text{MJy sr}^{-1}$  for the IRAS 60 and  $100 \mu\text{m}$ , SPIRE 250, 350 and  $500 \mu\text{m}$ , *Planck* 350, 550 and  $850 \mu\text{m}$  bands, respectively.

The instrumental uncertainty on the H I column density was directly estimated from the convolved ALFALFA maps, measuring the standard deviation of the featureless regions (fields V3 and V4) in the IVC map range. It is  $1.0 \times 10^{18} \text{ cm}^{-2}$  for both the IVC and LVC channels. For the typical emissivities found here, the contribution of instrumental noise in H I column density maps is smaller than that from FIR/submm images (reaching a maximum of  $0.005 \text{ MJy sr}^{-1}$  in the  $350 \mu\text{m}$  bands).

In all the dust emission maps we used, monochromatic flux densities were derived from wide band measurements assuming a flat spectrum,  $F_\nu \propto 1/\nu$ . We estimated color corrections assuming the average SED reconstructed using Eq. 1 as the *true* spectrum. They were found to be small, within less than 2% for most bands, with the exception of the *Planck*  $550 \mu\text{m}$  and  $850 \mu\text{m}$  bands. In the following, we only correct the results obtained on these bands, by multiplying them by a factor 0.9. A similar result can be obtained using the *Planck* color correction software (Planck Collaboration IX 2014) and assuming the *Planck* MBB fit to high latitude Galactic emission ( $T=20.3 \text{ K}$ ,  $\beta=1.59$ ; Planck Collaboration XI 2014).

## 4. Results

The parameters derived by fitting Eq. 1 to each image of dust emission, for each field, are given in Table 1, together with the errors estimated from the Monte Carlo analysis. The dust emission associated with LVC gas is estimated at a significant level in all fields and bands ( $\epsilon_\nu^{\text{LVC}} > 3\sigma$ ). In contrast, dust associated with IVC gas is significantly detected only in fields V1 and V2, while in fields V3 and V4  $\epsilon_\nu^{\text{IVC}} < 3\sigma$  in most cases (the only exceptions are the marginal detections in the two IRAS bands for V4). This was not unexpected, given the low column density of IVC gas in the two southernmost fields already shown in Fig. 3.

In Fig. 4 and 5 we show the pixel-by-pixel correlation between dust emission in the IRAS, SPIRE and *Planck*-HFI  $850 \mu\text{m}$  bands and column density of the two H I components, for fields V1/V2 and V3/V4, respectively. For each velocity channel, the surface brightness is corrected by subtracting the fitted contribution from the other velocity channel and the offset and ecliptic latitude gradient. Thus, for the LVC gas, the surface brightness on the y-axis is  $I_\nu - \epsilon_\nu^{\text{IVC}} \times N_{\text{H I}}^{\text{IVC}} - O_\nu - E_\nu \times (b - b_0)$ . The line and filled contours show the density of pixels before and after masking the regions deviant from the model by more than  $3\sigma_R$  at  $250\mu\text{m}$ ; the dashed and solid straight lines are the fitted correlation in the two cases (the slope of the solid line being one of the  $\epsilon_\nu$  values reported in Table 1). In some cases, masking removes regions with high gas column density where significant excess emission shows up as an upturn of the contour plots (see, e.g. the case for the LVC component at  $250 \mu\text{m}$  in V2); in others, it affects regions at lower column density. The possible nature of these residuals is discussed in Sect. 6. In any case, the effect of masking on the parameter derivation is marginal: the

**Table 1.** Dust emissivities  $\epsilon_v^{LVC}$  and  $\epsilon_v^{IVC}$  for the two H I components, offsets  $O_v$  and ecliptic latitude gradients  $E_v$ , derived for each field and band considered in this work. Errors are derived with the Monte Carlo technique described in Sect. 3. Estimates below  $3\sigma$  are in italics.  $\sigma_R$  is the standard deviation of the residuals  $R_v$ .  $\sigma_C$  is derived from  $\sigma_R$  after removing the contribution to the uncertainties due to instrumental noise in dust emission and H I maps. For  $\epsilon_v^{LVC}$  and  $\epsilon_v^{IVC}$ , the average over the fields is also reported (excluding low S/N values), together with its standard deviation.

	field	IRAS		Herschel - SPIRE			Planck - HFI		
		60 $\mu\text{m}$	100 $\mu\text{m}$	250 $\mu\text{m}$	350 $\mu\text{m}$	500 $\mu\text{m}$	350 $\mu\text{m}$	550 $\mu\text{m}$	850 $\mu\text{m}$
$\epsilon_v^{LVC}$ $10^{-20}$ MJy sr $^{-1}$ cm $^2$	V1	0.163 $\pm$ 0.012	0.774 $\pm$ 0.041	0.747 $\pm$ 0.045	0.341 $\pm$ 0.034	0.134 $\pm$ 0.024	0.399 $\pm$ 0.028	0.101 $\pm$ 0.012	0.0284 $\pm$ 0.0016
	V2	0.2051 $\pm$ 0.0089	0.773 $\pm$ 0.029	0.844 $\pm$ 0.037	0.414 $\pm$ 0.021	0.163 $\pm$ 0.011	0.462 $\pm$ 0.023	0.1288 $\pm$ 0.0066	0.03434 $\pm$ 0.00089
	V3	0.135 $\pm$ 0.014	0.680 $\pm$ 0.034	0.859 $\pm$ 0.039	0.415 $\pm$ 0.025	0.175 $\pm$ 0.011	0.484 $\pm$ 0.026	0.1495 $\pm$ 0.0098	0.0409 $\pm$ 0.0015
	V4	0.123 $\pm$ 0.025	0.508 $\pm$ 0.047	0.698 $\pm$ 0.061	0.412 $\pm$ 0.037	0.212 $\pm$ 0.022	0.486 $\pm$ 0.048	0.154 $\pm$ 0.019	0.0464 $\pm$ 0.0026
	avg.	0.157 $\pm$ 0.036	0.68 $\pm$ 0.12	0.787 $\pm$ 0.077	0.395 $\pm$ 0.036	0.171 $\pm$ 0.032	0.458 $\pm$ 0.041	0.133 $\pm$ 0.024	0.0375 $\pm$ 0.0078
$\epsilon_v^{IVC}$ $10^{-20}$ MJy sr $^{-1}$ cm $^2$	V1	0.245 $\pm$ 0.011	0.706 $\pm$ 0.029	0.447 $\pm$ 0.027	0.204 $\pm$ 0.022	0.059 $\pm$ 0.014	0.209 $\pm$ 0.020	0.0500 $\pm$ 0.0079	0.0139 $\pm$ 0.0012
	V2	0.228 $\pm$ 0.010	0.696 $\pm$ 0.027	0.370 $\pm$ 0.031	0.168 $\pm$ 0.020	0.0586 $\pm$ 0.0097	0.189 $\pm$ 0.022	0.0479 $\pm$ 0.0074	0.0123 $\pm$ 0.0012
	V3	<i>0.038<math>\pm</math> 0.071</i>	<i>0.37<math>\pm</math> 0.19</i>	<i>0.14<math>\pm</math> 0.19</i>	<i>0.06<math>\pm</math> 0.13</i>	<i>0.038<math>\pm</math> 0.057</i>	<i>-0.03<math>\pm</math> 0.12</i>	<i>-0.023<math>\pm</math> 0.049</i>	<i>-0.0002<math>\pm</math> 0.0073</i>
	V4	0.317 $\pm$ 0.066	0.51 $\pm$ 0.13	0.24 $\pm$ 0.23	0.26 $\pm$ 0.13	0.013 $\pm$ 0.073	0.13 $\pm$ 0.17	0.049 $\pm$ 0.059	0.0145 $\pm$ 0.0093
	avg.	0.263 $\pm$ 0.047	0.64 $\pm$ 0.11	0.408 $\pm$ 0.054	0.186 $\pm$ 0.026	0.05880 $\pm$ 0.00023	0.199 $\pm$ 0.014	0.0489 $\pm$ 0.0015	0.0131 $\pm$ 0.0011
$O_v$ MJy sr $^{-1}$	V1	0.201 $\pm$ 0.021	0.989 $\pm$ 0.063	-1.529 $\pm$ 0.064	-0.695 $\pm$ 0.047	-0.248 $\pm$ 0.031	0.238 $\pm$ 0.038	0.181 $\pm$ 0.016	0.0955 $\pm$ 0.0020
	V2	0.185 $\pm$ 0.018	1.051 $\pm$ 0.056	-1.677 $\pm$ 0.072	-0.811 $\pm$ 0.040	-0.314 $\pm$ 0.021	0.105 $\pm$ 0.044	0.113 $\pm$ 0.013	0.0811 $\pm$ 0.0019
	V3	0.231 $\pm$ 0.026	1.220 $\pm$ 0.054	-1.101 $\pm$ 0.068	-0.531 $\pm$ 0.043	-0.226 $\pm$ 0.017	0.188 $\pm$ 0.046	0.124 $\pm$ 0.016	0.0784 $\pm$ 0.0024
	V4	0.120 $\pm$ 0.033	1.303 $\pm$ 0.071	-0.97 $\pm$ 0.11	-0.619 $\pm$ 0.065	-0.286 $\pm$ 0.035	0.146 $\pm$ 0.079	0.101 $\pm$ 0.029	0.0667 $\pm$ 0.0043
	avg.	0.185 $\pm$ 0.021	1.141 $\pm$ 0.063	-1.254 $\pm$ 0.068	-0.691 $\pm$ 0.043	-0.269 $\pm$ 0.022	0.167 $\pm$ 0.044	0.127 $\pm$ 0.016	0.0784 $\pm$ 0.0024
$E_v$ MJy sr $^{-1}$ deg $^{-1}$	V1	-0.0206 $\pm$ 0.0036	-0.062 $\pm$ 0.011	0.029 $\pm$ 0.011	0.0303 $\pm$ 0.0091	0.0135 $\pm$ 0.0060	0.0472 $\pm$ 0.0068	0.0228 $\pm$ 0.0029	0.00909 $\pm$ 0.00033
	V2	-0.0021 $\pm$ 0.0039	-0.0006 $\pm$ 0.0096	-0.012 $\pm$ 0.012	-0.0116 $\pm$ 0.0079	-0.0042 $\pm$ 0.0044	0.0104 $\pm$ 0.0091	0.0009 $\pm$ 0.0033	0.00051 $\pm$ 0.00045
	V3	0.0769 $\pm$ 0.0034	0.0475 $\pm$ 0.0080	-0.0729 $\pm$ 0.0089	-0.0370 $\pm$ 0.0055	-0.0158 $\pm$ 0.0022	-0.0231 $\pm$ 0.0056	-0.0077 $\pm$ 0.0019	-0.00075 $\pm$ 0.00027
	V4	-0.0802 $\pm$ 0.0042	-0.0139 $\pm$ 0.0056	0.0154 $\pm$ 0.0077	0.0113 $\pm$ 0.0046	0.0081 $\pm$ 0.0031	0.0230 $\pm$ 0.0062	0.0066 $\pm$ 0.0025	0.00172 $\pm$ 0.00035
	avg.	-0.0011 $\pm$ 0.0036	-0.0011 $\pm$ 0.0096	-0.0011 $\pm$ 0.0089	-0.0011 $\pm$ 0.0055	-0.0011 $\pm$ 0.0022	0.0011 $\pm$ 0.0056	0.0011 $\pm$ 0.0019	0.0011 $\pm$ 0.00027
$\sigma_R(\sigma_C)$ MJy sr $^{-1}$	V1	0.048 (0.037)	0.11 (0.10)	0.14 (0.13)	0.10 (0.10)	0.061 (0.059)	0.10 (0.099)	0.057 (0.048)	0.037 (0.012)
	V2	0.049 (0.039)	0.13 (0.12)	0.16 (0.15)	0.096 (0.093)	0.054 (0.052)	0.11 (0.10)	0.057 (0.048)	0.037 (0.012)
	V3	0.047 (0.036)	0.097 (0.083)	0.12 (0.11)	0.087 (0.083)	0.050 (0.048)	0.093 (0.091)	0.057 (0.048)	0.037 (0.012)
	V4	0.045 (0.033)	0.088 (0.072)	0.11 (0.10)	0.083 (0.079)	0.050 (0.048)	0.091 (0.089)	0.054 (0.045)	0.037 (0.012)
	avg.	0.047 (0.036)	0.097 (0.083)	0.12 (0.11)	0.087 (0.083)	0.050 (0.048)	0.093 (0.091)	0.057 (0.048)	0.037 (0.012)

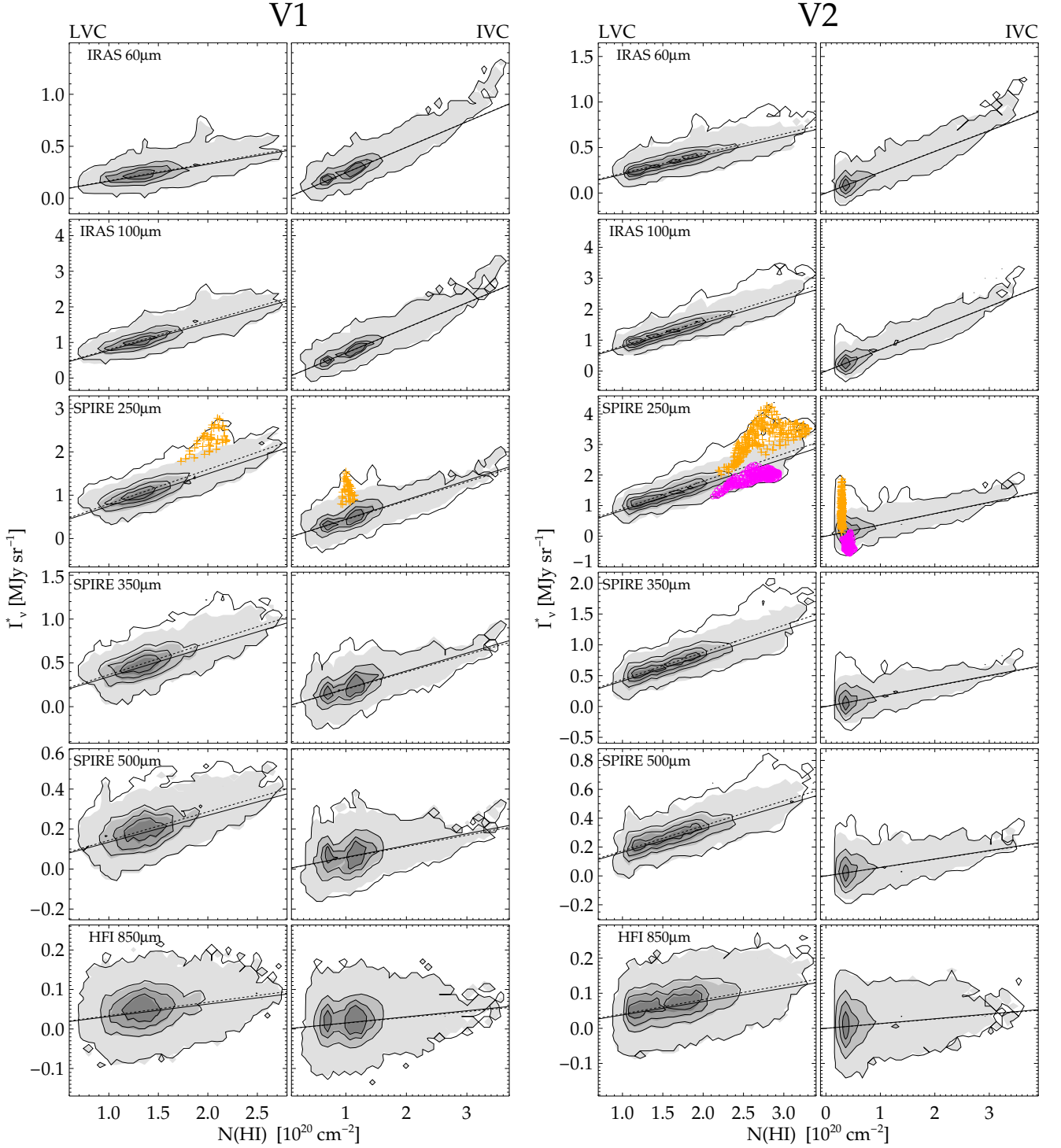


**Fig. 4.** Pixel-by-pixel correlation between dust emission and atomic gas column density, for field V1 and V2 in the IRAS, SPIRE and *Planck*-HFI 850 $\mu\text{m}$  bands. For the LVC (IVC) gas component, the dust surface brightness  $I_v^*$  is corrected to exclude the fitted contribution of the IVC (LVC) component; also, the offset and ecliptic latitude component is removed. Contours of constant pixel density enclosing 99.9, 75, 50 and 25% of the pixels are plotted. The gray-scale filled contours show the same after masking regions deviant from the model by more than  $3\sigma_R$  at 250  $\mu\text{m}$ . Solid and dashed lines show the fitted correlation before and after the masking, respectively. Small changes in the fitted  $O_v$ , before and after the masking result in slight displacements of the line and filled contours. Orange crosses in the 250 $\mu\text{m}$  panels refer to pixels within the isophotal ellipses of object 6 (in V1) and 14 (in V2). Magenta circles in the V2 250 $\mu\text{m}$  panels show region 'N' of negative residuals (see Sect. 6 for details).

emissivities derived without masking would be higher by up to a maximum of  $1.5\sigma$  (for the LVC component in fields V2 and V3 at 100 and 250  $\mu\text{m}$ ), with  $\sigma$  the uncertainty estimated from the Monte Carlo analysis. Nevertheless, Table 1 reports the values obtained after masking. The standard deviation of the resid-

uals  $\sigma_R$  is also reported in the table, together with  $\sigma_C$ , derived by removing from  $\sigma_R$  the contribution of instrumental noise in dust emission and gas column density observation. The value  $\sigma_C$  includes all deviations from the adopted model and should be dominated, for the low column density regions, by the fluctu-



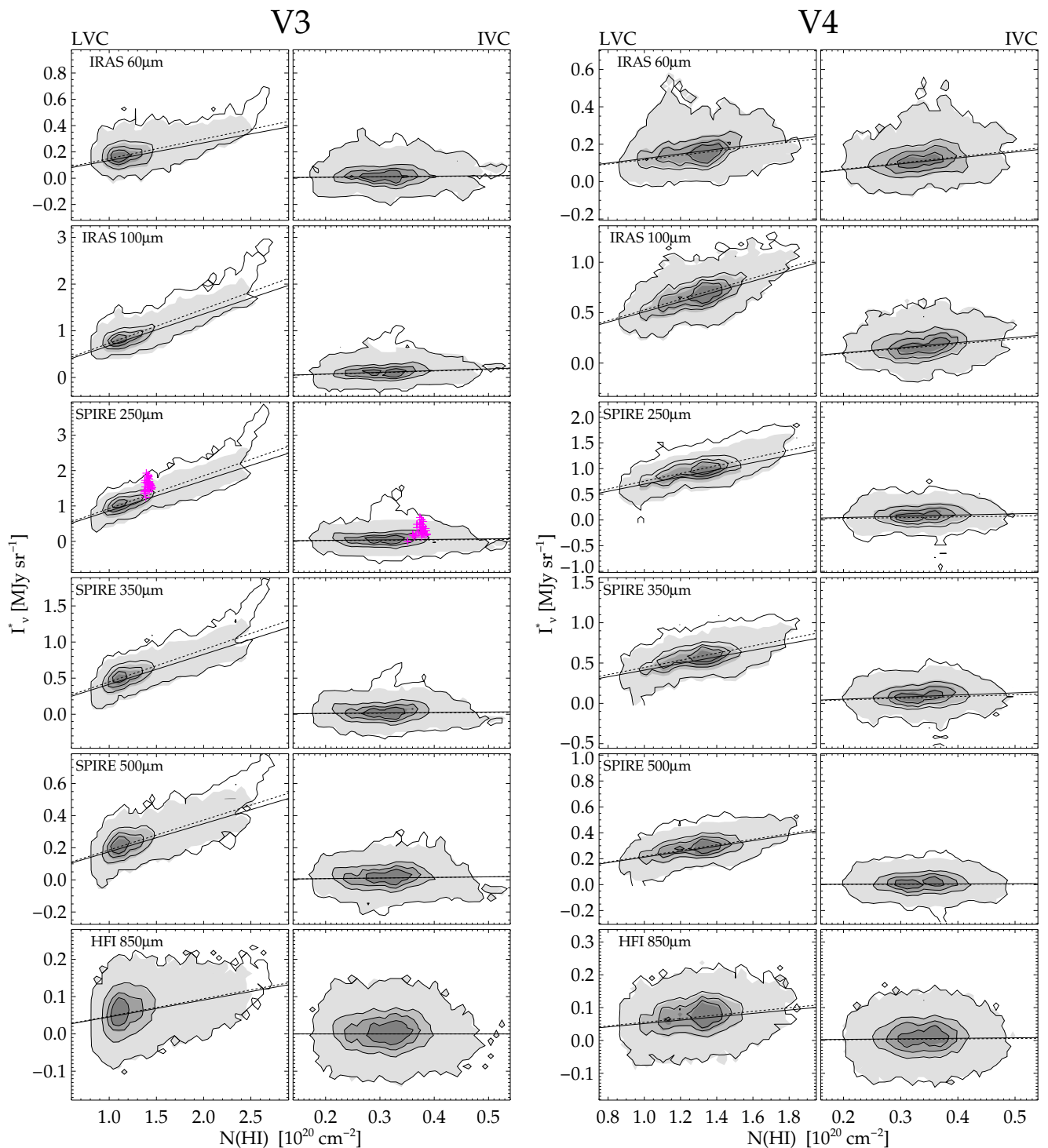


**Fig. 5.** Same as Fig. 4, but for field V3 and V4. Magenta crosses in the V3 250 $\mu\text{m}$  panels show the pixels of region 'G' (the galaxy VCC975; see Sect. 6 and footnote 4 for details).

ations in the CIB (Planck Collaboration XXIV 2011). Our estimates for  $\sigma_R$  (and  $\sigma_C$ ) are very close to those obtained at 100  $\mu\text{m}$  and in the *Planck* bands for low column density regions by Planck Collaboration XI (2014; see the first line in their table C.1); they indeed confirm that the standard deviation of the residuals is dominated by the CIB fluctuations at all bands, with the exception of 850 $\mu\text{m}$ , where the contribution of instrumental noise is larger.

In the rest of this text, we focus our attention on the results obtained for the dust emissivities associated to the two gas com-

ponents,  $\epsilon_v^{\text{LVC}}$  and  $\epsilon_v^{\text{IVC}}$ ; the discussion of the fitted offsets  $O_v$  and ecliptic latitude gradients  $E_v$  is presented in Appendix A. Fig. 6 shows the emissivity SED derived for each HeViCS field. The mean emissivities for the full HeViCS coverage are shown in Fig. 7 and reported in Table 1. The scatter (as measured by the standard deviation of the emissivities of the various field) is relatively small, generally below 15-20% of the mean value. This is however larger than the individual uncertainties of each estimate (typically in the range  $\sim 5\text{-}10\%$ ), pointing to real field-to-field variations in the emissivity values (see next section).

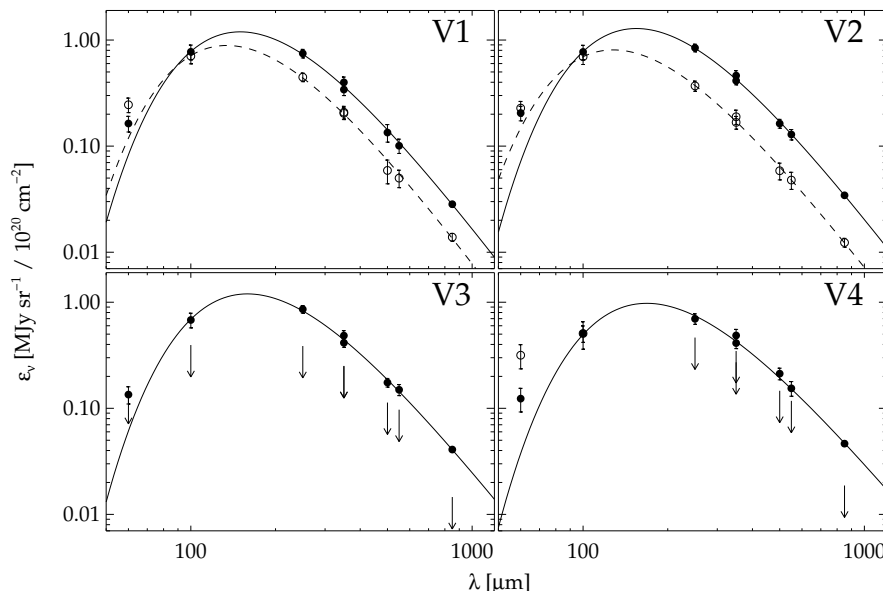


**Fig. 6.** Emissivities for the four HeViCS fields. Filled symbols and solid lines refer to the estimates for  $\epsilon_v^{\text{LVC}}$  and their (variable  $\beta$ ) MBB fits, respectively; open symbols, 2- $\sigma$  upper limits and dashed lines refer to  $\epsilon^{\text{LVC}}$ .

It is important to remember that, in order to compare our results with those in Planck Collaboration XI (2014), we scaled our ALFALFA map to match the LAB column densities (Sect. 2.1). If we had not done this, the derived emissivities would have been lower by 6% for the LVC component, a difference compatible with the estimated uncertainties in the emissivity derivation, corresponding to a maximum of  $1.5\sigma$  at  $100\ \mu\text{m}$ ; and by a larger amount, 14%, for the IVC component (equivalent to a maximum of  $3.5\sigma$  at  $100\ \mu\text{m}$ ). These differences are entirely due to the gain correction described in Sect. 2.1, since the offset between ALFALFA and LAB is negligible.

We found the SPIRE and *Planck* emissivities in the overlapping band at  $350\ \mu\text{m}$  to be marginally consistent, with a difference of about 1.5- $\sigma$  for the LVC component; the  $350\ \mu\text{m}$  SPIRE/*Planck* emissivity ratio is 0.86, which is entirely due to the relative gain of the SPIRE and *Planck* maps used in this work. Instead, the accurate analysis of Bertincourt et al. (2016) finds that the relative gain is close to unity. The difference cannot be accounted for by including color corrections (which we neglected at  $350\ \mu\text{m}$ ), nor by switching to the most recent releases of *Planck* and *Herschel* data. The use of the latest pipeline-reduced SPIRE  $350\ \mu\text{m}$  (downloaded from the Herschel Science Archive in August 2016) confirms our result. The reason for the difference is unknown. We are tempted to impute it to the peculiarities of the HeViCS fields. In fact, the HeViCS average surface brightness is at least a factor two smaller than that of the *Spider cirrus* molecular cloud, the lowest-intensity field used by Bertincourt et al. (2016); when our procedures for data manipulation and analysis are applied to pipeline-reduced SPIRE data of that target, we indeed obtain a result which is entirely consistent with their findings.

## 5. Absorption cross-sections of high latitude dust

The SED of diffuse high latitude dust is one of the test beds for Galactic dust models, because of two simplifying conditions: dust emission can be reasonably assumed to be optically thin in the diffuse medium; the line of sight at high latitude crosses a very limited range of dust environments, and a single heating source can be assumed, that provided by the LISRF.

A very simple description of dust emission is provided by a MBB: assuming that all dust grains share the same composition and size (and thus attain the same temperature  $T$  under the same heating conditions), the emissivity SED can be written as

$$\epsilon_v = \frac{\tau_v}{N_H} B_\nu(T).$$

The FIR/submm absorption cross section (per unit hydrogen atom) is usually described by a power law; adopting  $250\ \mu\text{m}$  as the reference wavelength, it can be written as

$$\frac{\tau_v}{N_H} = \frac{\tau(250\ \mu\text{m})}{N_H} \times (250\ \mu\text{m}/\lambda)^\beta.$$

A fit to the emissivity SEDs can thus retrieve the dust temperature  $T$  and the absorption cross section normalization  $\tau(250\ \mu\text{m})/N_H$  and spectral index  $\beta$ .

In general, a MBB results in an adequate fit to the observations, provided that datapoints contaminated by dust at hotter temperatures and/or not emitting at thermal equilibrium are excluded from the analysis (for this reason, the  $60\ \mu\text{m}$  emissivities are not included in the fits presented here). However, the parameters retrieved from the fits might be different from those of the underlying dust population. In particular, simultaneous solutions for  $T$  and  $\beta$  might be degenerate, since both quantities determines the SED shape. An inverse correlation between these parameters is generally found and imputed to a bias due to standard  $\chi^2$  minimization techniques, calling for more sophisticated Bayesian-fitting methods for a rigorous treatment of all involved uncertainties (see, e.g., Kelly et al. 2012); or to line-of-sight temperature mixing, even at high Galactic latitude (see, e.g., Veneziani et al. 2010; Bracco et al. 2011). Even when dust is heated by a single radiation field, grains attain different temperatures, depending on their size and composition: this broadens the SED, and biases the observed  $\beta$  to values smaller than the intrinsic spectral index of dust, in particular for radiation fields weaker than the LISRF (Hunt et al. 2015).

For the sake of simplicity, and in analogy to Planck Collaboration XXIV (2011) and Planck Collaboration XI (2014), we adopt here a single MBB model and fit it to the data for each field, and to the average emissivity, using a standard  $\chi^2$  minimization routine

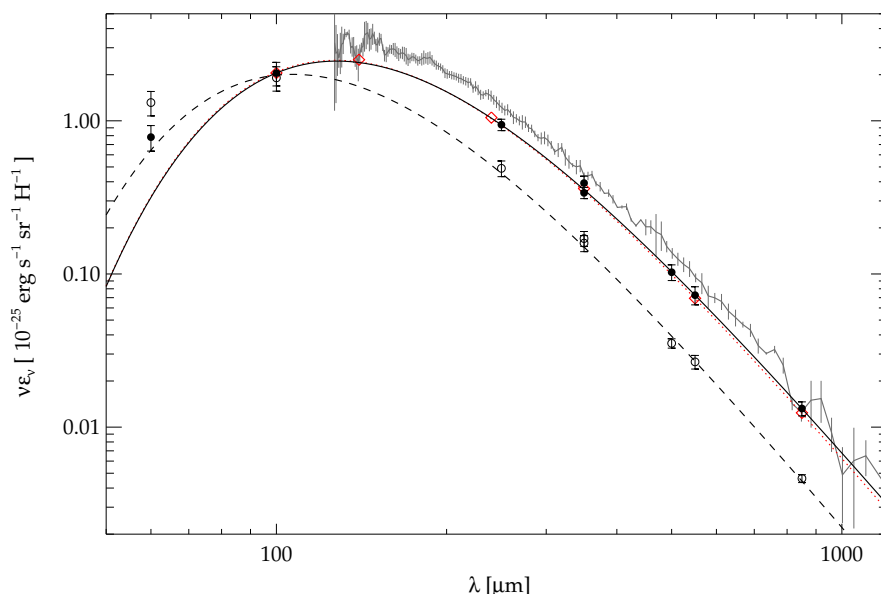


**Fig. 7.** Mean emissivities for the full HeViCS coverage. Filled circles and solid lines refer to the estimates for  $\epsilon^{\text{LVC}}$  and their (variable  $\beta$ ) MBB fits, respectively; open circles and dashed lines refer to  $\epsilon^{\text{IVC}}$ . The error bars show the standard deviation of the mean. The red squares are the COBE-DIRBE and Planck-HFI emissivities derived in the southern Galactic pole (Planck Collaboration Int. XVII 2014); the red dotted line is the fit to *Planck* high latitude emissivities (Planck Collaboration XI 2014); the gray line and error bars refer to the high latitude emissivities from FIRAS (Compiègne et al. 2011).

**Table 2.** Parameters of single temperature MBB fits to the emissivity SEDs

	V1	V2	V3	V4	avg.
LVC					
$\frac{\tau(250\mu\text{m})}{N_{\text{H1}}} / \frac{10^{-25}\text{cm}^2}{\text{H}}$	0.44±0.11	0.54±0.12	0.52±0.11	0.49±0.13	0.49±0.13
T/K	20.7±1.4	20.1±1.2	20.3±1.2	20.0±1.4	20.4±1.5
$\beta$	1.69±0.14	1.67±0.11	1.51±0.12	1.33±0.14	1.53±0.17
$\frac{\tau(250\mu\text{m})}{N_{\text{H1}}} / \frac{10^{-25}\text{cm}^2}{\text{H}}$	0.370±0.030	0.467±0.023	0.596±0.038	0.755±0.072	0.525±0.052
T/K	21.6±1.1	20.92±0.50	19.61±0.52	17.91±0.68	20.00±0.70
$\beta$			1.59 (fixed)		
IVC					
$\frac{\tau(250\mu\text{m})}{N_{\text{H1}}} / \frac{10^{-25}\text{cm}^2}{\text{H}}$	0.200±0.056	0.139±0.043	-	-	0.150±0.040
T/K	22.7±1.9	24.5±2.3	-	-	23.9±2.0
$\beta$	1.77±0.16	1.63±0.18	-	-	1.65±0.15
$\frac{\tau(250\mu\text{m})}{N_{\text{H1}}} / \frac{10^{-25}\text{cm}^2}{\text{H}}$	0.153±0.015	0.130±0.014	-	-	0.137±0.011
T/K	24.7±1.6	25.1±1.2	-	-	24.6±1.2
$\beta$			1.59 (fixed)		

(mpfit for IDL; Markwardt 2009); we allow  $\beta$  to vary (these fits are plotted in Fig. 6 and 7) but we also produce fits using a fixed  $\beta$ . The parameters derived from the fits are given in Table 2.

### 5.1. LVC dust

For dust associated with LVC gas, we find a trend of relatively higher emissivities at longer wavelengths in the two southernmost fields. This translates to fits with spectral index increasing from  $\beta \approx 1.3$  in field V4 to  $\beta \approx 1.7$  in field V1. Instead, the temperature is relatively constant in the four fields ( $T = 20.0 - 20.7\text{K}$ ). If instead  $\beta = 1.59$  is used, as derived by Planck Collaboration XI (2014) on the Diffuse High Galactic Latitude medium (DHGL, defined by  $b > 15^\circ$ ,  $N_{\text{H1}} < 5 \times 10^{20}\text{cm}^{-2}$ ; Compiègne et al. 2011), the fitted temperature reduces to 17.9K in field V4 and increases to 21.6K in field V1. This behavior is a clear effect of the T- $\beta$  degeneracy (Shetty et al. 2009).

The fit to the average emissivities, as well as the emissivities themselves, is consistent with the previous fit to the DHGL medium (red dotted line in Fig. 7). For a variable  $\beta$ , we find  $\tau(250\mu\text{m})/N_{\text{H}} = (0.49 \pm 0.13) \times 10^{-25}\text{cm}^2\text{H}^{-1}$ ,  $T = 20.4 \pm 1.5\text{K}$  and  $\beta = 1.53 \pm 0.17$ , while the Planck Collaboration XI (2014) values for the DHGL are  $\tau(250\mu\text{m})/N_{\text{H}} = (0.49 \pm 0.14) \times 10^{-25}\text{cm}^2\text{H}^{-1}$ ,  $T = 20.3 \pm 1.3\text{K}$  and  $\beta = 1.59 \pm 0.12$ . Analogous consistency is obtained by fitting the COBE-DIRBE and *Planck*-HFI emissivities of the south Galactic pole (red diamonds in Fig. 7; Planck Collaboration Int. XVII 2014):  $\tau(250\mu\text{m})/N_{\text{H}} = (0.55 \pm 0.05) \times 10^{-25}\text{cm}^2\text{H}^{-1}$ ,  $T = 19.8 \pm 1.0\text{K}$  and  $\beta = 1.65 \pm 0.10$ . The emissivities derived in this work are thus representative of the average properties of high latitude dust. This is remarkable, since the DHGL and the south Galactic pole medium cover 50% and 20% of the sky, respectively, while our fields are just  $\sim 0.2\%$ .

## 5.2. Implications for dust modelling

The *Herschel*-SPIRE emissivities derived in this work also share with *Planck*-HFI the inconsistency with the dust emission spectra obtained by the FIRAS instrument aboard the COBE satellite. The HFI team switched from a FIRAS- to a planet- (Uranus and Neptune) based calibration for the 350  $\mu\text{m}$  and 550  $\mu\text{m}$  bands, after recognising in the FIRAS data a bias of uncertain origin (Planck Collaboration VIII 2014). The FIRAS emissivity spectrum for the DHGL derived by Compiègne et al. (2011) is shown in Fig.7. As it has been pointed out, the new emissivities, confirmed here by the analysis of (Neptune-calibrated) SPIRE data, ask for a revision of the current models for MW dust, whose properties (grain composition and size distribution) were adjusted to reproduce the FIRAS spectrum (Planck Collaboration Int. XVII 2014; Planck Collaboration Int. XXIX 2016). For example, the MC10 dust model distributed with the DustEM software (Compiègne et al. 2011) reproduced FIRAS DHGL emissivities (after correcting them for the contribution of ionized gas -mostly, with a small correction for molecular gas- to the hydrogen column density) when heated by the LISRF. Using the new emissivities, the absorption cross-sections would need to be adjusted so that emission at, e.g., 250  $\mu\text{m}$ , is lower by 20%, the modelled SED shape for LISRF heating<sup>3</sup> being still consistent with observations (Planck Collaboration Int. XVII 2014).

In Appendix B we discuss the implications of these new absorption cross-sections in the determination of the dust masses of external galaxies.

## 5.3. IVC dust

Dust associated with IVC is found to have a lower emissivity than LVC dust (on average by about 1/2 at 250  $\mu\text{m}$ ) and a lower absorption cross-section. This result confirms the findings of Planck Collaboration XXIV (2011), which tentatively impute the different properties of IVC dust to a larger fraction of smaller grains not emitting at thermal equilibrium. Dust processing leading to smaller grain sizes (in particular grain shattering, dominant over gas-grain sputtering; Bocchio et al. 2014) is indeed expected in the shocked gas of Galactic fountains, which has been proposed as an explanation for the IVC medium (for a review, see, Wakker & van Woerden 1997). A lower opacity cross section, and a higher temperature than for LVC dust is found, for relatively similar  $\beta$  values. Assuming  $\beta = 1.59$ , the emissivity is  $\tau(250\mu\text{m})/N_{\text{H}} = (0.14 \pm 0.01) \times 10^{-25} \text{ cm}^2 \text{ H}^{-1}$  with  $T \approx 25\text{K}$ . Unfortunately, we cannot compare quantitatively our results with those obtained on LVC and IVC dust by Planck Collaboration XXIV (2011), since they used an earlier release of *Planck* data calibrated on FIRAS, and adopted the older FIRAS-based value  $\beta = 1.8$  for both dust components. We only note that the SED is *bluer* because of the different dust properties, rather than because of a heating source more intense

<sup>3</sup> Compiègne et al. (2011) used the standard formulation of Mathis et al. (1983) for the LISRF. Draine (2011) proposes a few modifications to it, in order to match COBE-DIRBE observations of diffuse stellar radiation in the near-infrared. Using the DustEM code and the MC10 dust model we estimated that the modified LISRF would increase the dust emissivity by about 10% (the net effect being that of increasing the original LISRF by about 25%). If this new estimate of the LISRF is adopted, new dust models should decrease their FIR output by 30% with respect to FIRAS. Also, colder dust temperatures would be required.

than the LISRF (the IVC medium being located higher above the Galactic plane than the LVC; Sect. 2.1).

## 6. Residuals

In Fig. 8 we show the observed dust emission, the dust emission modelled from the H I observations using the derived emissivities (Eq. 1), and the residuals in the SPIRE 250 $\mu\text{m}$  band. In order to show observations and models on the same scale, the large scale terms derived from the fit (offsets and ecliptic latitude gradients) have been subtracted from the images. For ease of presentations, the four HeViCS fields are combined in a single image by removing the small residual offsets between the fields (see Appendix. A); the analysis, though, was conducted separately on each field, as detailed in the previous Sections. Analogous figures for the other IRAS, SPIRE and HFI bands are shown in Appendix C.

Models and residuals shows consistent results in all bands. The 60  $\mu\text{m}$  residuals (Fig. C.1) are similar to those at 100  $\mu\text{m}$  (Fig. C.2), both IRAS bands having a similar contribution from dust associated to LVC and IVC gas (at least in the V1 and V2 areas). All SPIRE and HFI bands between 250  $\mu\text{m}$  and 850  $\mu\text{m}$  (Fig. 8, C.3 to C.7), where the LVC gas contribution to dust emission is at least twice that of IVC, show basically the same pattern in observations, models and residuals; the largest deviations from the models, though, more easily stand out in shorter wavelength bands, where they dominate over the background noise.

A visual comparison between data and models shows that, on large scales, there is a good correspondence between the features seen in dust and H I emission. We have already shown the good correlation between these two ISM tracers in Sect. 4. However, there are significant deviations at smaller scales: infrared emission appears less filamentary than H I, mostly because of the superimposition of the clumpier CIB to the cirrus; (some) regions of high H I column density have infrared emission much in excess of those predicted by the model.

### 6.1. A catalog of excess regions

We have identified the main excess regions by running the source extraction software *sExtractor* (Bertin & Arnouts 1996) on the 250  $\mu\text{m}$  residual maps. We selected all sources with pixel values above  $3\sigma_R$  and with size larger than a beam (about 12 pixels).

To avoid fragmentation, the mask of bright background sources was unset. An initial source list was produced, and pruned of those objects whose isophotal ellipses included a significant contribution from background objects, both masked and unmasked<sup>4</sup>. This contribution was estimated by making mock images of the extragalactic sources, including the Virgo cluster galaxies detected at 250 $\mu\text{m}$  by Auld et al. (2013) (assuming for simplicity they can be described by point sources at the adopted resolution) and the objects in the HeViCS SPIRE point source

<sup>4</sup> About half of the Virgo Cluster galaxies detected by Auld et al. (2013) were not masked. The brightest is VCC975, with a flux of 1.1 Jy at 250  $\mu\text{m}$ . It is shown by the magenta circle marked with 'G' in Fig. 8; the corresponding pixels are plotted as crosses on the 250  $\mu\text{m}$  V3 panels in Fig. 5. Beside the obvious results that galaxy-dominated pixels have no correlation with foreground gas column densities, the panels show that even for the brightest source the contribution to the emissivity determination is limited: only pixels on the peak of the galaxy have been excluded from the fit.

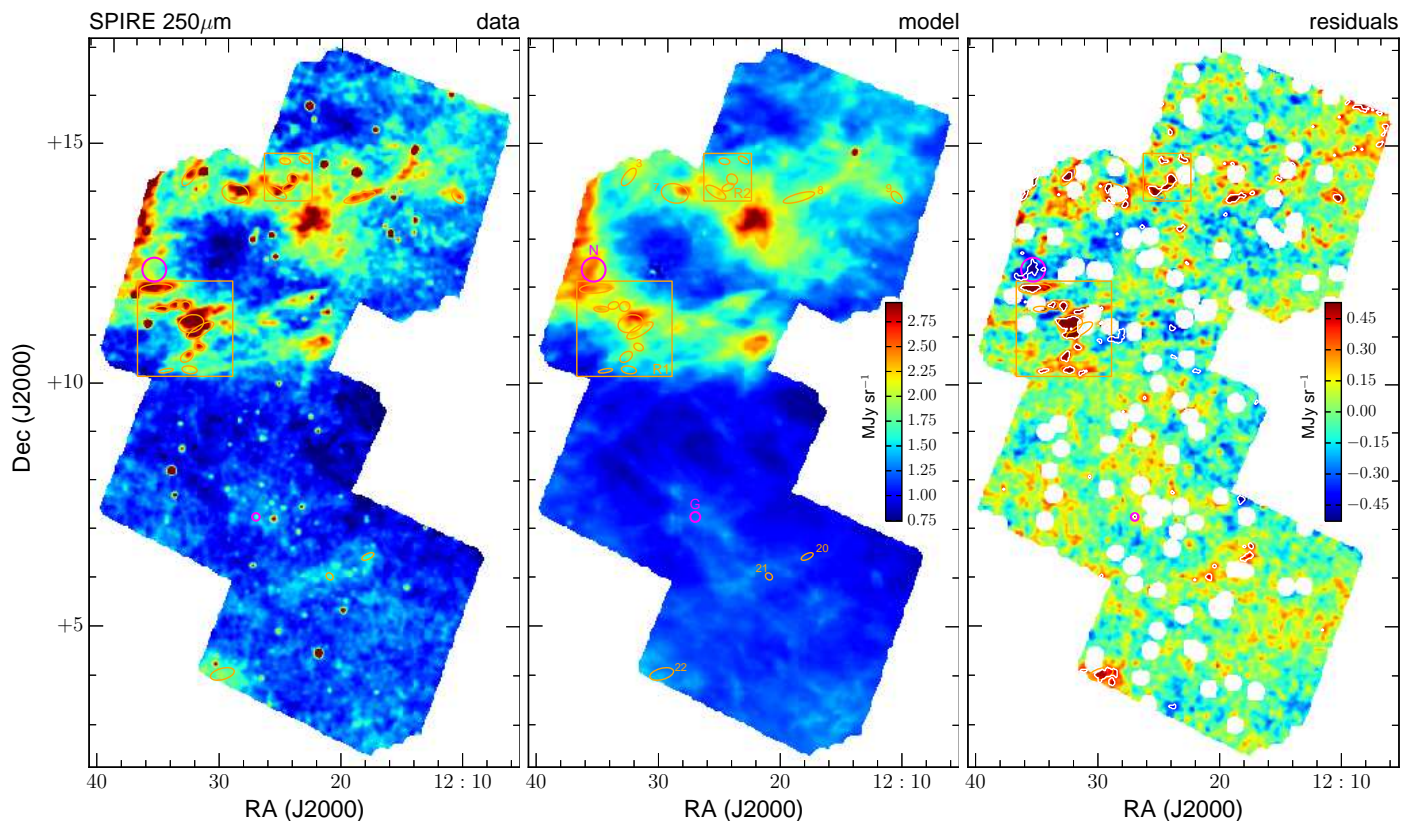


**Fig. 8.** Observations (left column), models (middle column) and residuals (right column) of the HeViCS field in the SPIRE 250 $\mu$ m band. Observations and models have been subtracted by the large scale terms  $O_v + E_v \times (b - b_0)$  and are shown on the same color scale. The color scale of the residuals goes from  $-4$  to  $4\sigma_R$  (Table 1); round white areas show the object mask applied before the fitting, while white contours encircle the regions where residuals are larger than  $3\sigma_R$  (excluded during the fitting). The orange numbered ellipses and square regions refers to the high positive residual regions listed in Table 3 and shown in Fig. 9. The magenta circle labelled 'N' highlights a region with high negative residuals; that labelled 'G' is centered on an unmasked Virgo Cluster galaxy.

catalog of Pappalardo et al. (2015)<sup>5</sup>. To keep contamination low, we only retained objects where the contribution from galaxies was smaller than 20% the total residual.

The final catalog is shown in Table 3, where for each object we list the center, semi-major axis, axis ratio and position angle of the major axis of the isophotal ellipses, together with the median and peak residuals within the isophote. The remaining columns will be described in the following. Isophotal ellipses are shown in the maps of Fig. 8. Individual objects or group of objects are also shown in Fig. 9, overlaid on the 250  $\mu$ m map at the original resolution (FWHM $\approx$ 18"), providing a better view of the morphology of diffuse emission.

<sup>5</sup> The few tens of thousands point sources measured in the catalog produce, when smoothed to the adopted resolution, a map characterized by fluctuations over an average background. By histogram fitting we estimated values of  $0.106 \pm 0.041$ ,  $0.074 \pm 0.033$  and  $0.027 \pm 0.020$  MJy sr $^{-1}$  for the average background and fluctuations at 250, 350 and 500  $\mu$ m. When compared to estimates of the CIB (Gispert et al. 2000), these average values show that detected point sources contribute to only a fraction of it (up to 15% at 250  $\mu$ m; see also Béthermin et al. 2012). Also, the background fluctuations inferred from resolved sources are smaller than the  $\sigma_C$  values found in this work (Table 1), which are mostly due to undetected sources, together with the large residuals from the foreground cirrus modelling. When estimating the contribution of point sources to the excess regions, we neglected the average value, which should be accounted for in the constant offsets  $O_v$ .

## 6.2. A few examples

A large group of high-residual regions is present in the V2 tile, near to (and partly in correspondence with) the overlap with V3 (we define this region R1 in Figs. 8 and 9). It consists of several clouds interconnected by a filamentary structure, whose surface brightness peaks have been masked during the emissivity determination in all but the 850  $\mu$ m image. The object with the largest residual is # 14 of Table 3. The pixels within its isophotal ellipse are shown as crosses in the 250 $\mu$ m dust-HI correlation panels for V2 (Fig. 4). The excess is clearly associated with the higher column density LVC gas (appearing as excess emission for the lowest density IVC gas in the field), though however the region does not lay exactly on the local LVC peak (the maximum being at the edge of the ellipse, as shown in the middle panel of Fig. 8). Similar excesses have been found in a recent work by Reach et al. (2015), who study the correlation between HI column density from the Arecibo GALFA survey and dust emission from *Planck*. Our work is analogous to theirs, though the column densities of the HeViCS fields are smaller than those of the high latitude clouds studied by Reach et al. (2015). They argue that the residuals could be produced by: different local dust properties; a local increase of the ISM density not traced by  $N_{\text{HI}}$ , due to the presence of molecular gas; an underestimation of  $N_{\text{H}}$  due to the neglect of HI self-absorption. We examine these alternatives below.

**Table 3.** Excess regions at 250  $\mu\text{m}$ 

	RA [°]	Dec [°]	a [']	b/a	PA [°]	$R_v$ [MJy sr <sup>-1</sup> ]		$\epsilon_v^{\text{LVC}} _{\text{ex}} / \epsilon_v^{\text{LVC}}$		$N_{\text{H}_2}$ [cm <sup>-2</sup> ]		$\tau$	
						median	peak	median	peak	median	peak	median	peak
1	185.823746	14.725930	7.2	0.50	57	0.50	0.70	1.4	1.5	3.4e+19	4.7e+19	0.9	1.2
2	186.240067	14.695560	6.8	0.57	80	0.45	0.57	1.3	1.4	3.0e+19	3.8e+19	0.8	1.0
3	188.306244	14.343020	13.2	0.44	141	0.45	0.90	1.2	1.4	2.7e+19	5.3e+19	0.6	1.1
4	186.421265	14.043010	14.4	0.39	58	0.46	0.94	1.3	1.6	3.1e+19	6.3e+19	0.8	1.4
5	186.071487	14.318910	7.2	0.87	48	0.60	1.00	1.4	1.6	4.0e+19	6.7e+19	1.0	1.5
6	186.156967	14.151900	8.0	0.51	112	0.71	1.08	1.5	1.7	4.8e+19	7.2e+19	1.1	1.6
7	187.308731	14.012690	17.1	0.70	76	0.52	1.33	1.3	1.6	3.1e+19	7.9e+19	0.7	1.5
8	184.624084	13.942280	20.3	0.24	105	0.46	0.72	1.3	1.5	3.1e+19	4.8e+19	0.8	1.2
9	182.506973	13.937320	9.1	0.55	42	0.45	0.78	1.4	1.6	3.0e+19	5.2e+19	0.9	1.5
10	188.974243	11.995280	20.4	0.28	93	0.50	0.92	1.2	1.4	3.0e+19	5.4e+19	0.5	0.9
11	188.348526	11.628510	6.6	0.93	107	0.58	0.87	1.3	1.4	3.4e+19	5.1e+19	0.7	1.0
12	188.587433	11.647190	6.8	0.66	106	0.49	0.78	1.2	1.4	2.9e+19	4.6e+19	0.6	0.9
13	188.841675	11.567190	9.4	0.38	89	0.45	0.73	1.2	1.3	2.7e+19	4.3e+19	0.5	0.8
14	188.217331	11.272350	15.9	0.68	104	0.77	1.80	1.3	1.8	4.5e+19	1.1e+20	0.8	1.8
15	188.014572	11.132850	18.8	0.32	119	0.92	1.49	1.4	1.7	5.4e+19	8.8e+19	1.1	1.6
16	188.038177	10.786410	6.3	0.71	62	0.49	0.69	1.2	1.3	2.9e+19	4.1e+19	0.6	0.8
17	188.299667	10.578530	8.9	0.63	126	0.50	0.83	1.3	1.5	3.0e+19	4.9e+19	0.7	1.1
18	188.235886	10.306960	9.5	0.50	81	0.44	0.75	1.3	1.5	2.6e+19	4.5e+19	0.8	1.3
19	188.732086	10.282890	9.1	0.26	99	0.42	0.52	1.3	1.4	2.5e+19	3.1e+19	0.9	1.0
20	184.445099	6.452250	8.2	0.42	116	0.40	0.48	1.4	1.6	2.9e+19	3.4e+19	1.1	1.4
21	185.244553	6.040510	4.9	0.80	42	0.40	0.48	1.4	1.5	2.9e+19	3.4e+19	1.0	1.2
22	187.458755	4.039970	15.4	0.45	105	0.41	0.52	1.4	1.4	2.9e+19	3.7e+19	0.9	1.1

### 6.2.1. Different dust properties

If one assumes that the LVC H<sub>I</sub> column density is a faithful tracer of the full ISM density, the pixel-by-pixel correlation of the excess emission could be explained by the contribution of dust at higher emissivity than that for the diffuse medium. However, it is not straightforward to derive the increase in emissivity without knowing the fraction of the total gas column density that is associated with the more emissive dust. If the whole column density under the excess area is associated with dust at a higher emissivity  $\epsilon_v^{\text{LVC}}|_{\text{ex}}$ , the residuals can be written as the difference between the emission of this dust and the emission that is predicted from the whole field,

$$R_v = \epsilon_v^{\text{LVC}}|_{\text{ex}} N_{\text{H}_1} - \epsilon_v^{\text{LVC}} N_{\text{H}_1},$$

which leads to

$$\frac{\epsilon_v^{\text{LVC}}|_{\text{ex}}}{\epsilon_v^{\text{LVC}}} = 1 + \frac{R_v}{\epsilon_v^{\text{LVC}} N_{\text{H}_1}}.$$

At 250  $\mu\text{m}$ , the excess area has residuals values  $R_v = 0.77$  and 1.8 MJy sr<sup>-1</sup> for the average and for the peak, respectively, that would correspond to a moderate increase in emissivity by a factor of 1.3 to 1.8. In principle, this higher emissivity can be simply due to a larger dust temperature in the excess region with respect to the average temperature derived from the full field. However, the SED of the residuals within the area is consistent with a temperature close to the average temperature of the field ( $T=20.4\text{K}$  for  $\beta = 1.59$ , to be compared with  $T=20.5\pm 0.5$  for field V2; see Fig. 10).

For the same temperature, a higher emissivity corresponds to a higher dust absorption cross-section. Larger dust cross-sections are found in dense Milky Way clouds: for example Juvela et al. (2015) measured the absorption cross-sections in Galactic cold cores using *Planck* and *Herschel* data, finding values up to more than three times those of the diffuse medium. The larger cross-section can result from grain growth due to accretion of gas atoms (C, H) into mantles (Ysard et al. 2015; Köhler et al. 2015), to the formation of ice

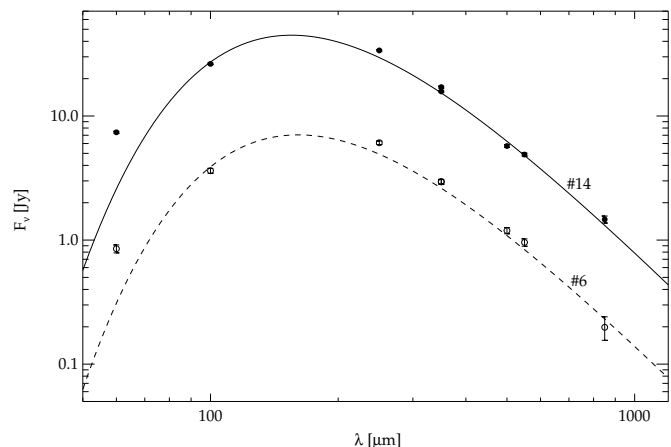


**Fig. 10.** The SED of object 14 in field V2 and 6 in V1. Errorbars for each aperture have been estimated from  $\sigma_R$  (Table 1). Modified blackbody fits assume  $\beta = 1.59$  and exclude the 60  $\mu\text{m}$  data.

mantles, and to the coagulation of grains (Ossenkopf & Henning 1994; Köhler et al. 2015). However, our excess regions lack the main characteristic defining dense Galactic cold clouds, i.e. the lower temperature with respect to the surrounding medium. Also, Galactic cold clumps have on average higher column densities (Planck Collaboration XXIII 2011); none of the sources of the *Planck* Catalogue of Galactic Cold Clumps (Planck Collaboration XXVIII 2016) falls within the HeViCS footprint.

### 6.2.2. Molecular gas

Conversely, if one assumes that the dust properties do not change significantly in the limited column density range of the HeViCS fields, the excess could be explained by untraced molecular gas. Indeed, excess emission over the dust/H<sub>I</sub> correlation has been used to detect molecular clouds (see, e.g., Desert et al. 1988;

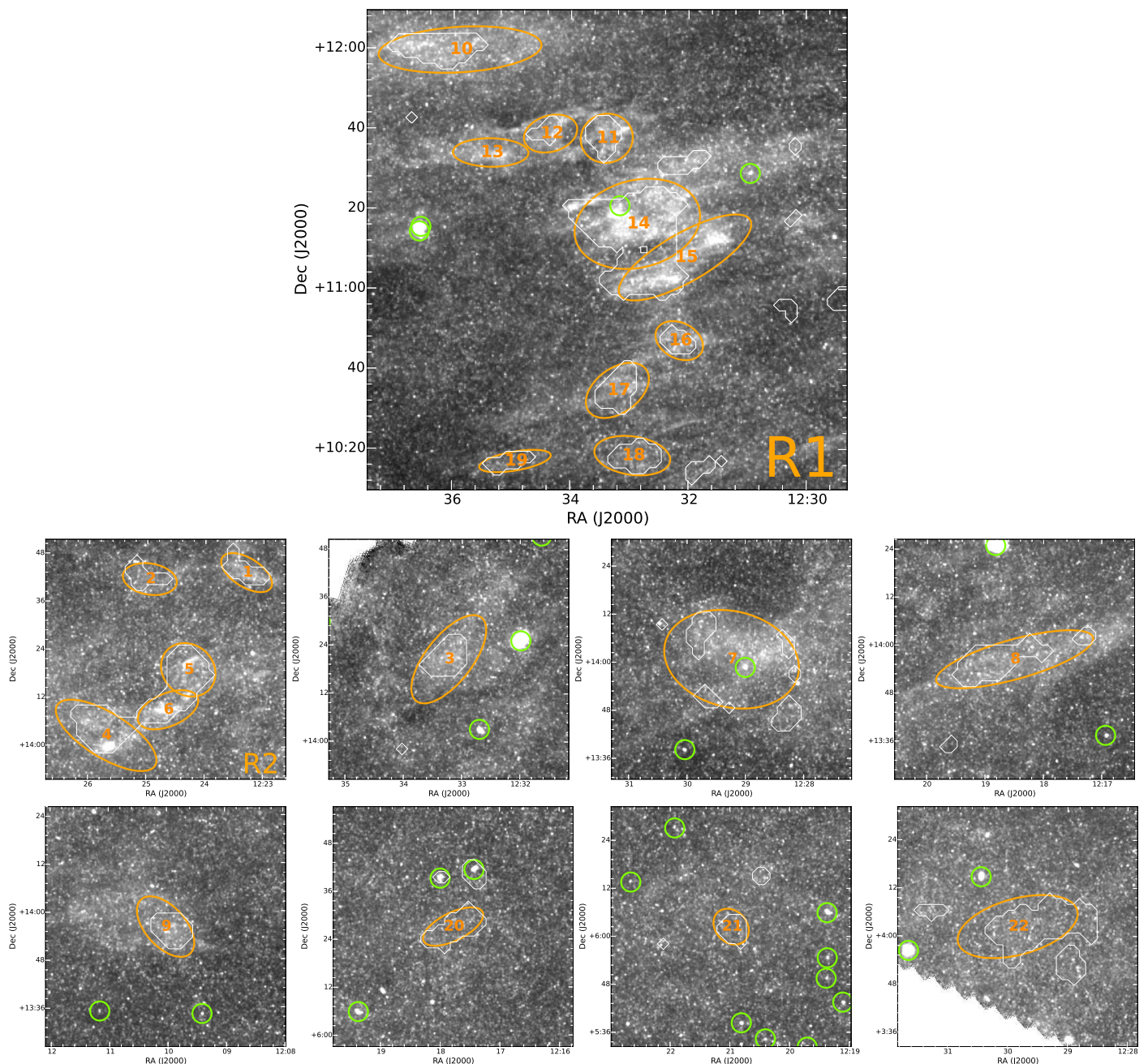


**Fig. 9.** Regions with high positive residuals, superimposed on the SPIRE 250  $\mu\text{m}$  map at the original resolution. For each object detected by *sExtractor*, isophotal ellipses are shown (see Table 3). White contours correspond to regions masked during the emissivity determination. Green circles (diameter = 2 FWHM) show the VCC galaxies detected by Auld et al. (2013). The size of the R1 panel is  $2^\circ \times 2^\circ$ ,  $1^\circ \times 1^\circ$  for all the others.

Reach et al. 1998). Due to the limited resolution of available surveys, these searches only detected larger excesses than those measured here: for instance, the region we are considering is marked by low surface brightness contours in the 100  $\mu\text{m}$  excess map of the north Galactic pole in Reach et al. (1998) and has not been included in their final catalog of detected clouds.

Adopting the same emissivity as for atomic gas, the residuals could be used to derive the column density of untraced H nucleons, and thus to estimate the  $\text{H}_2$  column density,

$$N_{\text{H}_2} = \frac{1}{2} \frac{R_{\nu}}{\epsilon_{\nu}^{\text{LVC}}}.$$

For the average and peak column densities of LVC gas in the excess area one should expect a molecular gas column density

ranging from  $N_{\text{H}_2} = 0.4$  to  $1.1 \times 10^{20} \text{ cm}^{-2}$ . Unfortunately, there are no molecular gas surveys at high Galactic latitude sensitive enough to detect these column density levels. The HeViCS area has been covered by the North Galactic Hemisphere CO(1-0) survey of Hartmann et al. (1998), with a sparsely sampled  $\sim 1^\circ \times 1^\circ$  grid. However, in none of the pointings was CO emission detected, with a  $2\text{-}\sigma$  upper limit corresponding to  $N_{\text{H}_2} = 1.2 \times 10^{20} \text{ cm}^{-2}$  (assuming the typical velocity width of the clouds detected in the survey and the standard  $X_{\text{CO}} = 2 \times 10^{20} \text{ cm}^{-2} (\text{K km s}^{-1})^{-1}$  conversion factor for Galactic molecular clouds; Bolatto et al. 2013). Besides having a detection limit close to that inferred from our highest excess region, the grid of pointings (with beam FWHM = 8'.4) misses all regions with high residuals. The fully sampled CO(1-0) map derived from *Planck* observations can-

not be of help either, being featureless within the HeViCS footprint (we used the type-3 map of Planck Collaboration XIII 2014); it also has a  $2\text{-}\sigma$  upper limit 4 times higher than that of Hartmann et al. (1998).

Gillmon & Shull (2006) studied the correlation between IRAS surface brightnesses and molecular gas column densities derived from UV absorption lines in a sample of high-latitude AGNs; they concluded that significant fractions of  $\text{H}_2$  are present in most diffuse cirrus clouds. Unfortunately, the limited dynamic range of our residuals does not help in understanding if the excess regions are just the tip of diffuse molecular clouds or isolated cores ( $3\text{-}\sigma_R$  corresponding to about  $0.3 \times 10^{20} \text{ cm}^{-2}$ , a third of the estimate for the peak value). Molecular gas with  $N_{\text{H}_2} \approx 2 - 3 \times 10^{20} \text{ cm}^{-2}$  was detected by Cortese et al. (2010) in correspondence to a  $5'$  plume to the north of the interacting pair NGC4435/NGC4438 and interpreted as a compact cirrus cloud (the plume is detected in HeViCS images, but it is masked in our analysis due to the proximity to the bright galaxies). Compact molecular clouds with  $N_{\text{H}_2} \lesssim 1 \times 10^{20} \text{ cm}^{-2}$  have been found in a few limited fields at high Galactic latitude (Small Area Molecular Structures - SAMS; Heithausen 2002, 2007). Dust emission associated with SAMS has been detected in SPIRE images (Heithausen 2012), and indeed for one of them dust emissivity in excess of that for the diffuse medium has been reported (Davies et al. 2010b). The SAMS studied so far are however smaller, with typical sizes of  $1\text{-}2'$ ; yet they tend to be grouped in clusters (Heithausen 2007). Thus, our excess region, which appears more extended and filamentary also at the original  $250 \mu\text{m}$  resolution could be a web of connected SAMS. Heithausen (2002) claims that SAMS are transitory objects, as they are not sufficiently shielded from UV radiation to survive for long time (Heithausen 2002, 2007). Yet, Gillmon & Shull (2006) found that  $\text{H}_2$  self-shielding can already occur for  $N_{\text{H}_2} \gtrsim 10^{18} \text{ cm}^{-2}$  in regions with  $I_\nu \gtrsim 2 \text{ MJy sr}^{-1}$  at  $100 \mu\text{m}$ . These surface brightness levels are indeed consistent with those found here.

### 6.2.3. $\text{H I}$ self-absorption

Instead, if the excess is due to the neglect of  $\text{H I}$  self-absorption in the estimate of the gas column density, the total  $\text{H I}$  column density should be 30 to 80% larger than what is actually measured in the optically thin limit for LVC gas (the estimate depending on the use of average or peak values, respectively). The optical depth at the line center would need to range between 0.8 and 1.8 to explain the excess (Eq. 15 in Reach et al. 2015). These optical depths are larger than those derived from  $\text{H I}$  absorption (see Sect. 2.1); yet, none of the probed lines-of-sight falls on a high residual region. The values estimated here are smaller than those derived in the higher density regions analyzed by Reach et al. (2015); even if they are seldom encountered at high Galactic latitude (less than 4% of  $b > 30^\circ$  lines of sight in Heiles & Troland 2003, have higher optical depths) the coverage fraction of the residuals makes this hypothesis compatible with the absorption line observations. However, it is not clear why the excess in object # 14 should be due to  $\text{H I}$  self-absorption, while the peak of  $N_{\text{H I}}^{\text{LVC}}$  (at the northern edge of the selected area) does not show a similarly high residual.

Summarizing, we have no elements to favour one of the proposed explanations for the excesses over the other. We are tempted to exclude  $\text{H I}$  self-absorption, because of the mismatch between high column densities and high optical depth estimates; and to favour the molecular gas explanation, because of the de-

tection of similar column densities in other fields. Also, the latter hypothesis could be more readily tested with future dedicated observations of molecular lines over the areas of the excess regions.

As another example, we have considered a region in tile V1, (R2 in Figs. 8 and 9). It consists of a few clumps, three of which are aligned over a filament. Among them we have chosen source 6 of Table 3. As for the previous example, the SED (dashed line in Fig. 10) is compatible with dust at a temperature ( $T=19.7\text{K}$ ) very close to the field average. The pixel-by-pixel correlation is shown by the symbols in the  $250 \mu\text{m}$  panel for field V1 in Fig. 4. The excess is again associated with LVC gas, though not with the highest column densities available in the field. The residuals range from  $R_\nu = 0.7$  (median) to  $1.1 \text{ MJy sr}^{-1}$  (peak), which could result from either a dust emissivity a factor 1.5 to 1.7 higher than the average for the V1 field, to the presence of molecular gas with column density  $N_{\text{H}_2} = 0.5$  to  $0.7 \times 10^{20} \text{ cm}^{-2}$ , or to a  $\text{H I}$  line central optical depth between 1.1 and 1.6.

The properties of the other excess regions in the field are similar. For all the sources we have computed the change in dust emissivity, the  $\text{H}_2$  column density, or the  $\text{H I}$  opacity which could explain the residuals: these calculations are included in Table 3.

### 6.3. Negative residuals

So far, we discussed only the case of high positive residuals. There are, however, regions with negative residuals, in some cases so large (in absolute value) that they have been masked during the emissivity estimate. One such case is indicated by the red circle labelled 'N' in Fig. 8 ( $\text{RA}=189.02458^\circ$ ,  $\text{dec}=12.389513^\circ$ ), whose pixels are shown as diamonds in the V2  $250\mu\text{m}$  panel of Fig. 4. The negative residual corresponds to a  $15' \times 30'$  cloud in the LVC map, sharing the same velocity range as the neighborhood. The structure is a moderate enhancement of the neighboring gas column density, with  $N_{\text{H}} \approx 0.5 \times 10^{20} \text{ cm}^{-2}$  on top of a "background" column density  $N_{\text{H}} = 2.3 \times 10^{20} \text{ cm}^{-2}$ . Most of the diffuse emission in the area comes from dust associated with this background, and this explains why the selected pixels in Fig. 4 still show the same correlation as for the diffuse field. However, the emissivity is significantly lower than the mean: these residuals could be either explained by the absence of dust in the cloud (the *missing* emission indeed corresponds to the amount of dust one would expect from the  $\text{H I}$  density enhancement for the average field emissivity) or to a much smaller emissivity than the field, resulting from a colder dust temperature in the cloud. Although both interpretation are heuristically similar, a colder dust temperature seems to be excluded, since the negative residuals in this area can be seen also at the longer wavelengths.

At a lower level, negative (and positive) residuals can be found in all fields and bands, as expected from the scatter in the  $I_\nu / N_{\text{H}}$  correlation and from the anisotropies of the CIB (see, e.g. Planck Collaboration XXX 2014). A curious case is, however, that of the V2 field, where a large area of negative residuals is present, coincidentally, around the center of the background Virgo cluster and inside of the cirrus ring feature. This is shown in Fig. 11, where we plot the profiles of the 100 and  $250\mu\text{m}$  residuals as a function of the projected distance from the galaxy M87, at the center of the cluster (black lines), and we compare them with the flatter profiles obtained with the respect to the center in each of the other three HeViCS tiles (the gray lines and error bars show their average and standard deviation). The lower surface brightness inside the ring feature, when compared to the average level outside of it (in V2 and in the southern HeViCS



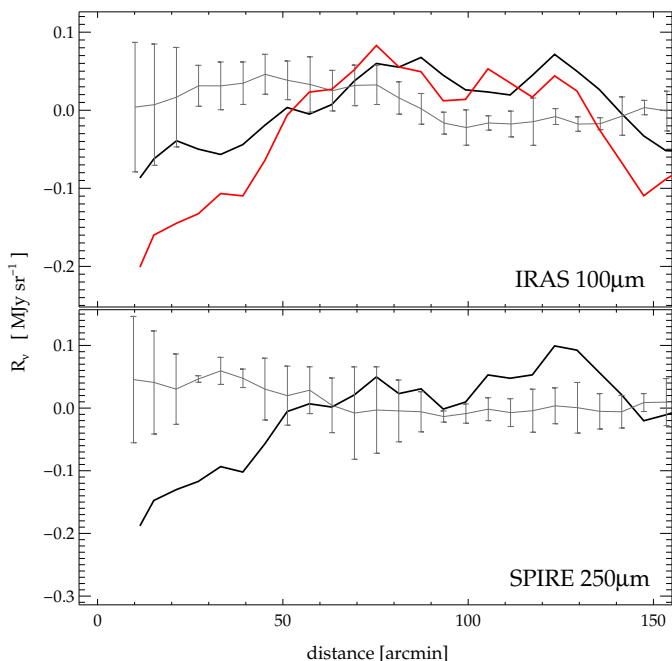


**Fig. 11.** Profile of the 100 and 250  $\mu\text{m}$  residuals as a function of the projected distance from M87 for the V2 field (black solid line). The gray lines and error bars are the average and standard deviation of the profiles from the center of each of the other three HeViCS tiles. The red solid line is the profile at 100  $\mu\text{m}$  predicted from the 250  $\mu\text{m}$  data and assuming the average 100/250 color ratio (see text for details). Each profile have been obtained by azimuthally averaging the residuals over circular coronas of width  $6'$ .

tiles), appears as a "hole". Its presence was recognised from the first HeViCS analysis, and was later evident also in the full sky IRAS and *Planck* surveys, from 100  $\mu\text{m}$  to 550  $\mu\text{m}$ .

It is not straightforward to understand whether this residual is due to a local large-scale underdensity in the CIB, or to different dust properties: if the reason is the latter, the residual could result from a lower emissivity (and thus lower cross-section, since the temperature estimated within  $1^\circ$  from M87,  $T=20.8\text{K}$  for  $\beta = 1.59$ , is very close to that for the LVC component) in a region with low gas column density ( $N_{\text{H I}} \approx 10^{20} \text{ cm}^{-2}$  for the LVC). This is in contrast, however, with the *excess* of emissivity seen at IRAS and *Planck* wavelength for  $N_{\text{H}} < 10^{20} \text{ cm}^{-2}$ , which could be due to variations in the dust composition and size distribution at the lower column densities (Ysard et al. 2015), or to the contribution of dust associated with diffused ionised gas (Planck Collaboration XI 2014). On the contrary, the "hole" could be due to H II-associated dust (which we did not account for in our analysis; Sect. 3) *only* if the column density of ionised gas is smaller inside of the feature than outside of it. However, the feature would appear as a significant dearth of H $\alpha$  emission even in the available large-scale surveys such as WHAM (Haffner et al. 2003), which is not the case.

## 7. Upper limits on intra-cluster dust emission

Despite the topic might seem out of the scope of this paper, one of the aim of HeViCS (and of the cirrus analysis) was the detection of emission from dust in the ICM. Dust grains could be removed from cluster galaxies and transported to the ICM by the same environmental processes (such as ram pressure stripping and tidal interaction; for a review, see Boselli & Gavazzi 2006)

which remove their gas content, or by internal process, such as global galactic winds (Popescu et al. 2000). The dust passed to the ICM could in principle be detected by its reddening of background galaxies and QSOs. There is a long history of attempts at detecting such cluster reddening, but the results are still controversial and inconclusive (for instance, compare the detection claimed by McGee & Balogh 2010 with the absence of significative excess reddening in Gutiérrez & López-Corredoira 2014).

A key issue is the ability of dust to survive destruction in the hot ICM gas (Dwek et al. 1990). For the Virgo cluster, when only environmental processes are considered, FIR emission would come predominantly from dust produced in the winds of evolved stars (Popescu et al. 2000). In this case, the predicted surface brightness is very low,  $0.01 \text{ MJy sr}^{-1}$  at 100  $\mu\text{m}$ . However, in a less prohibitive scenario, in which dust is injected by galactic winds, a larger FIR contribution could come from galaxies originally on the outskirts of the cluster and falling towards the center. If the dust is able to infall within  $1^\circ$  from M87, it could produce levels up to  $\lesssim 0.1 \text{ MJy sr}^{-1}$  at 175  $\mu\text{m}$  (case B of Popescu et al. 2000).

The complex structure of the residuals around M87, and in particular the large scale negative feature discussed in Sect. 6.3, makes it complicate to detect ICM dust in Virgo. In fact, contamination from the foreground cirrus has long been recognised to be the limiting factor in detecting diffuse FIR emission from clusters (Wise et al. 1993; Stickel et al. 2002; Bai et al. 2007; Kitayama et al. 2009).

Following Stickel et al. (1998), we have attempted to measure an excess in Virgo at 100  $\mu\text{m}$  with respect to 250  $\mu\text{m}$ . We used the 250  $\mu\text{m}$  V2 map to estimate the 100  $\mu\text{m}$  emission that would be expected on the basis of the average 100/250 color ratio (1.025, measured on field V2). This estimate is shown by the red line in Fig. 11. Indeed, the profile of the *true* residuals reveals a 100  $\mu\text{m}$  emission in excess of the predicted one. The excess is  $\approx 0.1 \text{ MJy sr}^{-1}$  in the cluster center, a value close to the detection claimed by Stickel et al. (1998) in Coma; to the models of Dwek et al. (1990) for the Coma cluster; and to the more optimistic predictions of intracluster dust emission in Virgo by Popescu et al. (2000). It is also close, however, to the upper limits of  $0.06 \text{ MJy sr}^{-1}$  estimated using *Spitzer* data at 70 and 160  $\mu\text{m}$  by Kitayama et al. (2009), who dismissed the dust detection in the Coma cluster by Stickel et al. (1998) as due to cirrus contamination. We are not able therefore to confirm that the excess is due to cluster emission, since it is of the same order as the noise in the residuals and in the random profiles centered on the other fields (gray lines and error bars in Fig. 11) which are caused by both variations in the dust emissivity and by the variance of the CIB (Planck Collaboration XI 2014). The issue is further complicated by the decorrelation between the 100  $\mu\text{m}$  CIB power spectrum and that at longer wavelengths (Planck Collaboration XXX 2014).

Notably, most of the truly intergalactic features (optically highlighted by Mihos et al. 2005) cannot be seen in dust emission. The only exception is the plume to the north of NGC4435/NGC4438 which Cortese et al. (2010) found to be most likely a foreground cirrus cloud rather than a tidal tail in the cluster. In fact, the only features of the deep optical survey of Virgo presented by Mihos (2015) clearly associated with emission in our maps are those corresponding to the highest column densities of the Galactic H I.

## 8. Summary and conclusions

We have studied the correlation between FIR emission and atomic gas column density for the low density, high Galactic latitude cirrus in the foreground of the Virgo Cluster. For the dust emission, we used the HeViCS maps at 250, 350 and 500  $\mu\text{m}$  obtained with the SPIRE instrument aboard the *Herschel* Space Observatory (Davies et al. 2010a, 2012; Auld et al. 2013); maps at 60 and 100  $\mu\text{m}$  obtained from the IRAS-IRIS dataset (Miville-Deschênes & Lagache 2005) and HFI maps at 350, 550 and 850  $\mu\text{m}$  from the 2013 *Planck* data release (Planck Collaboration I 2014). Two H I column density maps were obtained from the ALFALFA survey (Giovannelli et al. 2005), separating an IVC component with emission at velocities in the range  $-100 < v_{\text{LSR}} / \text{km s}^{-1} < -20$  and a LVC component with  $-20 < v_{\text{LSR}} / \text{km s}^{-1} < 100$ . For each band and for each of the four HeViCS fields, we have derived the dust emissivity associated with the two gas components. Our results can be summarised as follows:

- The values of the emissivities we found for dust associated with the LVC are consistent with the determinations by Planck Collaboration XI (2014) and Planck Collaboration Int. XVII (2014). In the SPIRE bands we measure  $\epsilon_{\nu}^{\text{LVC}} = (0.787 \pm 0.077)$ ,  $(0.395 \pm 0.034)$  and  $(0.171 \pm 0.032) \times 10^{-20} \text{ MJy sr}^{-1} \text{ cm}^2$  at 250, 350 and 500  $\mu\text{m}$ , respectively. The values represent the average and the standard deviation of the emissivities derived for each of the  $\approx 4^\circ \times 4^\circ$  HeViCS fields. The scatter in the emissivity values is generally larger than the uncertainties estimated for each individual field and points toward intrinsic field-to-field variations. Indeed, the scatter measured in the analysis of *Planck* data (covering a much larger range of column density than HeViCS) suggests variation of the dust properties along different lines of sight and environments (Ysard et al. 2015; Fanciullo et al. 2015). Yet it is remarkable that the average values derived for the HeViCS footprint, covering just 0.2% of the sky, are in excellent agreement (see Fig. 7) with the analysis of high latitude dust emission by the *Planck* team, covering from 20% (Planck Collaboration Int. XVII 2014) to 50% (Planck Collaboration XI 2014) of the sky.
- By fitting the average emissivity SED with a MBB, we derived a dust absorption cross-section

$$\frac{\tau_{\nu}^{\text{LVC}}}{N_{\text{H I}}} = (0.49 \pm 0.13) \times \left( \frac{250 \mu\text{m}}{\lambda} \right)^{1.53 \pm 0.17} \times 10^{-25} \text{ cm}^2 \text{ H}^{-1}$$

with an average dust temperature  $T = 20.4 \pm 1.5 \text{ K}$ . Again, this is consistent with the values derived by Planck Collaboration XI (2014) and Planck Collaboration Int. XVII (2014). In particular the planet-calibrated SPIRE data confirms the lower emissivity, absorption cross-section (and spectral index) with respect to the FIRAS spectrum and calls for a revisitation of the FIRAS-calibrated dust models (like, e.g., Draine 2003; Zubko et al. 2004; Compiègne et al. 2011; Jones et al. 2013). Nevertheless, we found that the dust absorption cross-section used in most of the HeViCS papers results in only a slight underestimate of the dust mass in a galaxy with respect to those obtained with the value above ( see Appendix B).

- Dust associated with the IVC component has lower emissivity than the LVC component,  $\epsilon_{\nu}^{\text{IVC}} = (0.408 \pm 0.054)$ ,  $(0.186 \pm 0.026)$  and  $(0.0588 \pm 0.00023) \times 10^{-20} \text{ MJy sr}^{-1} \text{ cm}^2$

at 250, 350 and 500  $\mu\text{m}$ ; it also has a bluer spectrum, resulting in a hotter dust temperature when fitted with a MBB, and in a lower dust cross-section. These results confirm the early analysis of *Planck* data for high latitude clouds, and point towards different properties of dust in the IVC with respect to the LVC (Planck Collaboration XXIV 2011).

- The high resolution of the ALFALFA data allowed us to study the departure of the H I-dust correlation at scales smaller than  $\sim 20'$ . This corresponds to (uncertain) linear sizes of 0.6 – 0.9 pc, assuming as a distance the scale-height of the global MW emission from cold dust (100 pc Misiriotis et al. 2006) or the scaleheight of the H I disk (150 pc Kalberla & Kerp 2009), respectively. We found regions with residuals significantly higher than the average scatter of the correlation. The high residual regions are most probably the result of local variation in the dust properties (increase in the dust emissivity by 20 to 80%) or excess emission associated with the small molecular clouds of average column density  $N_{\text{H}_2} \lesssim 10^{20} \text{ cm}^{-2}$ . We also found regions of negative residuals, and in particular a H I feature of the LVC component with no associated dust emission. This parcel of gas devoid of dust seems to suggest that, besides changes in the grain composition and size distribution, the scatter in the emissivity measurements could be due to an imperfect spatial correspondence between the ISM tracers at these smaller scales; on the other hand, dedicated observations of molecular gas tracers are needed to see if the excess emission can be due to (so far) untraced gas or to dust clouds devoid of a gas component.
- Due to the cirrus contamination and large residuals in the proximity of the center of the the Virgo cluster, we find no strong evidence for dust emission from the ICM. In fact, even for the most optimistic prediction for the Virgo cluster (Popescu et al. 2000) the surface brightness is not likely to exceed  $\approx 0.1 \text{ MJy sr}^{-1}$  at 100  $\mu\text{m}$ , a level which is the same as the average scatter of the residuals, dominated in most cases by CIB fluctuations.

This work was dedicated to the study of the cirrus absorption properties in the FIR/submm. The availability of deep UV (Boissier et al. 2015), optical (Ferraese et al. 2012; Mihos 2015) and atomic gas (Giovannelli et al. 2005; Peek et al. 2011) surveys of the Virgo cluster will also allow in the future a study of the emissivity of scattered starlight, thus posing further constraints on the dust grain models for the high Galactic latitude cirrus.

*Acknowledgements.* We are grateful to Edvige Corbelli, Luca Cortese, Emmanuel Xilouris and an anonymous referee for comments that improved the quality of the paper. S. B., J. I. D., M. Baes, M. Bocchio, V. C., C. J. R. C., A. J., S. M. acknowledge support from the European Research Council (ERC) in the form of the FP7 project DustPedia (P.I. Jonathan Davies, proposal 606824). S. B., C. G., L. K. H. are grateful for support from PRIN-INAF 2012/13. The ALFALFA team at Cornell was supported by the NSF grants AST-0607007 and AST-1107390 to R. G. and M. H. and by grants of the Brinson Foundation to M.H. S.Z. has been supported by the EU Marie Curie Career Integration Grant "SteMaGE" Nr. PCIG12-GA-2012-326466 (Call Identifier: FP7-PEOPLE-2012 CIG). Based on observations obtained with *Planck* (<http://www.esa.int/Planck>), an ESA science mission with instruments and contributions directly funded by ESA Member States, NASA, and Canada. This research has made use of: APLpy, an open-source plotting package for Python hosted at <http://aplpy.github.com>; the NASA/IPAC Extragalactic Database (NED) which is operated by the Jet Propulsion Laboratory, California Institute of Technology, under contract with the National Aeronautics and Space Administration; NASA's Astrophysics Data System.

## References

- Auld, R., Bianchi, S., Smith, M. W. L., et al. 2013, *MNRAS*, 428, 1880
- Bai, L., Rieke, G. H., & Rieke, M. J. 2007, *ApJL*, 668, L5
- Bertin, E. & Arnouts, S. 1996, *A&AS*, 117, 393
- Bertin, E., Mellier, Y., Radovich, M., et al. 2002, in *Astronomical Society of the Pacific Conference Series*, Vol. 281, *Astronomical Data Analysis Software and Systems XI*, ed. D. A. Bohlender, D. Durand, & T. H. Handley, 228
- Bertincourt, B., Lagache, G., Martin, P. G., et al. 2016, *A&A*, 588, A107
- Béthermin, M., Le Floch, E., Ibert, O., et al. 2012, *A&A*, 542, A58
- Bianchi, S. 2013, *A&A*, 552, A89
- Bianchi, S., Davies, J. I., & Alton, P. B. 2000, *A&A*, 359, 65
- Bocchio, M., Jones, A. P., & Slavin, J. D. 2014, *A&A*, 570, A32
- Bocchio, M., Jones, A. P., Verstraete, L., et al. 2013, *A&A*, 556, A6
- Boissier, S., Boselli, A., Voyer, E., et al. 2015, *A&A*, 579, A29
- Bolatto, A. D., Wolfire, M., & Leroy, A. K. 2013, *ARA&A*, 51, 207
- Boselli, A., Ciesla, L., Buat, V., et al. 2010a, *A&A*, 518, L61
- Boselli, A., Ciesla, L., Cortese, L., et al. 2012, *A&A*, 540, A54
- Boselli, A., Eales, S., Cortese, L., et al. 2010b, *PASP*, 122, 261
- Boselli, A. & Gavazzi, G. 2006, *PASP*, 118, 517
- Boulanger, F., Abergel, A., Bernard, J.-P., et al. 1996, *A&A*, 312, 256
- Boulanger, F. & Perault, M. 1988, *ApJ*, 330, 964
- Bracco, A., Cooray, A., Veneziani, M., et al. 2011, *MNRAS*, 412, 1151
- Clark, C. J. R., Schofield, S. P., Gomez, H. L., & Davies, J. I. 2016, *MNRAS*, 459, 1646
- Compiègne, M., Verstraete, L., Jones, A., et al. 2011, *A&A*, 525, A103
- Condon, J. J., Cotton, W. D., Greisen, E. W., et al. 1998, *AJ*, 115, 1693
- Cortese, L., Bendo, G. J., Isaak, K. G., Davies, J. I., & Kent, B. R. 2010, *MNRAS*, 403, L26
- Dale, D. A., Aniano, G., Engelbracht, C. W., et al. 2012, *ApJ*, 745, 95
- Davies, J. I., Baes, M., Bendo, G. J., et al. 2010a, *A&A*, 518, L48
- Davies, J. I., Bianchi, S., Cortese, L., et al. 2012, *MNRAS*, 419, 3505
- Davies, J. I., Wilson, C. D., Auld, R., et al. 2010b, *MNRAS*, 409, 102
- Desert, F. X., Bazell, D., & Boulanger, F. 1988, *ApJ*, 334, 815
- Désert, F. X., Boulanger, F., & Puget, J. L. 1990, *A&A*, 237, 215
- Draine, B. T. 2003, *ARA&A*, 41, 241
- Draine, B. T. 2011, *Physics of the Interstellar and Intergalactic Medium* (Princeton University Press)
- Draine, B. T., Dale, D. A., Bendo, G., et al. 2007, *ApJ*, 663, 866
- Draine, B. T. & Lee, H. M. 1984, *ApJ*, 285, 89
- Dwek, E., Rephaeli, Y., & Mather, J. C. 1990, *ApJ*, 350, 104
- Fanciullo, L., Guillet, V., Aniano, G., et al. 2015, *A&A*, 580, A136
- Ferriere, L., Côté, P., Cuillandre, J.-C., et al. 2012, *ApJS*, 200, 4
- Finkbeiner, D. P. 2003, *ApJS*, 146, 407
- Gillmon, K. & Shull, J. M. 2006, *ApJ*, 636, 908
- Giovanelli, R., Haynes, M. P., Kent, B. R., et al. 2005, *AJ*, 130, 2598
- Giovanelli, R., Haynes, M. P., Kent, B. R., et al. 2007, *AJ*, 133, 2569
- Gispert, R., Lagache, G., & Puget, J. L. 2000, *A&A*, 360, 1
- Griffin, M. J., Abergel, A., Abreu, A., et al. 2010, *A&A*, 518, L3
- Gutiérrez, C. M. & López-Corredoira, M. 2014, *A&A*, 571, A66
- Haffner, L. M., Reynolds, R. J., Tufte, S. L., et al. 2003, *ApJS*, 149, 405
- Hartmann, D., Magnani, L., & Thaddeus, P. 1998, *ApJ*, 492, 205
- Heiles, C. & Troland, T. H. 2003, *ApJS*, 145, 329
- Heithausen, A. 2002, *A&A*, 393, L41
- Heithausen, A. 2007, in *Astronomical Society of the Pacific Conference Series*, Vol. 365, *SINS - Small Ionized and Neutral Structures in the Diffuse Interstellar Medium*, ed. M. Haverkorn & W. M. Goss, 177
- Heithausen, A. 2012, *A&A*, 543, A21
- Helou, G. & Walker, D. W., eds. 1988, *Infrared astronomical satellite (IRAS) catalogs and atlases. Volume 7: The small scale structure catalog*, Vol. 7
- Hunt, L. K., Draine, B. T., Bianchi, S., et al. 2015, *A&A*, 576, A33
- James, A., Dunne, L., Eales, S., & Edmunds, M. G. 2002, *MNRAS*, 335, 753
- Jones, A. P., Fanciullo, L., Köhler, M., et al. 2013, *A&A*, 558, A62
- Juvela, M., Ristorcelli, I., Marshall, D. J., et al. 2015, *A&A*, 584, A93
- Kalberla, P. M. W., Burton, W. B., Hartmann, D., et al. 2005, *A&A*, 440, 775
- Kalberla, P. M. W. & Kerp, J. 2009, *ARA&A*, 47, 27
- Kelly, B. C., Shetty, R., Stutz, A. M., et al. 2012, *ApJ*, 752, 55
- Kitayama, T., Ito, Y., Okada, Y., et al. 2009, *ApJ*, 695, 1191
- Köhler, M., Ysard, N., & Jones, A. P. 2015, *A&A*, 579, A15
- Kuntz, K. D. & Danly, L. 1996, *ApJ*, 457, 703
- Lagache, G., Abergel, A., Boulanger, F., Désert, F. X., & Puget, J. L. 1999, *A&A*, 344, 322
- Lagache, G., Haffner, L. M., Reynolds, R. J., & Tufte, S. L. 2000, *A&A*, 354, 247
- Low, F. J., Young, E., Beintema, D. A., et al. 1984, *ApJL*, 278, L19
- Magrini, L., Bianchi, S., Corbelli, E., et al. 2011, *A&A*, 535, A13
- Markwardt, C. B. 2009, in *Astronomical Society of the Pacific Conference Series*, Vol. 411, *Astronomical Data Analysis Software and Systems XVIII*, ed. D. A. Bohlender, D. Durand, & P. Dowler, 251
- Mathis, J. S., Mezger, P. G., & Panagia, N. 1983, *A&A*, 128, 212
- McGee, S. L. & Balogh, M. L. 2010, *MNRAS*, 405, 2069
- Mihos, C. 2015, in *IAU Symposium No. 317, 2015, Vol. 22, The General Assembly of Galaxy Halos*
- Mihos, J. C., Harding, P., Feldmeier, J., & Morrison, H. 2005, *ApJL*, 631, L41
- Misiriotis, A., Xilouris, E. M., Papamastorakis, J., Boumris, P., & Goudis, C. D. 2006, *A&A*, 459, 113
- Miville-Deschênes, M. & Lagache, G. 2005, *ApJS*, 157, 302
- Neugebauer, G., Habing, H. J., van Duinen, R., et al. 1984, *ApJ*, 278, L1
- Ossenkopf, V. & Henning, T. 1994, *A&A*, 291, 943
- Ott, S. 2010, in *ASP Conference Series*, Vol. 434, 139
- Pappalardo, C., Bendo, G. J., Bianchi, S., et al. 2015, *A&A*, 573, A129
- Peek, J. E. G., Heiles, C., Douglas, K. A., et al. 2011, *ApJS*, 194, 20
- Pilbratt, G. L., Riedinger, J. R., Passvogel, T., et al. 2010, *A&A*, 518, L1
- Planck Collaboration I. 2014, *A&A*, 571, A1
- Planck Collaboration Int. XVII. 2014, *A&A*, 566, A55
- Planck Collaboration Int. XXIX. 2016, *A&A*, 586, A132
- Planck Collaboration Int. XXV. 2015, *A&A*, 582, A28
- Planck Collaboration IX. 2014, *A&A*, 571, A9
- Planck Collaboration VIII. 2014, *A&A*, 571, A8
- Planck Collaboration XI. 2014, *A&A*, 571, A11
- Planck Collaboration XII. 2014, *A&A*, 571, A12
- Planck Collaboration XIII. 2014, *A&A*, 571, A13
- Planck Collaboration XIV. 2014, *A&A*, 571, A14
- Planck Collaboration XXIII. 2011, *A&A*, 536, A23
- Planck Collaboration XXIV. 2011, *A&A*, 536, A24
- Planck Collaboration XXVIII. 2016, *A&A*, in press
- Planck Collaboration XXX. 2014, *A&A*, 571, A30
- Poglitsch, A., Waelkens, C., Geis, N., et al. 2010, *A&A*, 518, L2
- Popescu, C. C. & Tuffs, R. J. 2013, *MNRAS*, 436, 1302
- Popescu, C. C., Tuffs, R. J., Fischera, J., & Völk, H. 2000, *A&A*, 354, 480
- Reach, W. T., Heiles, C., & Bernard, J.-P. 2015, *ApJ*, 811, 118
- Reach, W. T., Wall, W. F., & Odegard, N. 1998, *ApJ*, 507, 507
- Rudick, C. S., Mihos, J. C., Harding, P., et al. 2010, *ApJ*, 720, 569
- Schlegel, D. J., Finkbeiner, D. P., & Davis, M. 1998, *ApJ*, 500, 525
- Shetty, R., Kauffmann, J., Schnee, S., & Goodman, A. A. 2009, *ApJ*, 696, 676
- Smith, M. W. L. 2012, PhD thesis, Cardiff University
- Smith, M. W. L., Vlahakis, C., Baes, M., et al. 2010, *A&A*, 518, L51
- Spitzer, L. 1978, *Physical Processes in the Interstellar Medium* (New York: Wiley)
- Stickel, M., Klaas, U., Lemke, D., & Mattila, K. 2002, *A&A*, 383, 367
- Stickel, M., Lemke, D., Mattila, K., Haikala, L. K., & Haas, M. 1998, *A&A*, 329, 55
- Veneziani, M., Ade, P. A. R., Bock, J. J., et al. 2010, *ApJ*, 713, 959
- Wakker, B. P. 2001, *ApJS*, 136, 463
- Wakker, B. P. & van Woerden, H. 1997, *ARA&A*, 35, 217
- Wise, M. W., O'Connell, R. W., Bregman, J. N., & Roberts, M. S. 1993, *ApJ*, 405, 94
- Witt, A. N., Gold, B., Barnes, III, F. S., et al. 2010, *ApJ*, 724, 1551
- Ysard, N., Köhler, M., Jones, A., et al. 2015, *A&A*, 577, A110
- Zubko, V., Dwek, E., & Arendt, R. G. 2004, *ApJS*, 152, 211

## Appendix A: Offsets and Zodiacal light gradients

We discuss here the offsets  $O_V$  and the ecliptic latitude gradient  $E_V$  resulting from the fitting described in Sect. 3 and 4.

The derived  $O_V$  are shown in the left panel of Fig. A.1. For the IRIS 60  $\mu\text{m}$ , the offset is positive, small, and very similar for all fields. At 100  $\mu\text{m}$ , it is larger and likely dominated by uncertainties in the subtraction of the zodiacal light contribution from IRIS maps: this is discussed in Planck Collaboration XI (2014), where a correction is found by comparing smoothed IRIS images with the earlier 100  $\mu\text{m}$  maps from Schlegel et al. (1998), which implemented a different, empirical, zodiacal light subtraction. When this correction is taken into account, our values of  $O_V$  are compatible with those derived by Planck Collaboration XI (2014) by correlating dust emission and atomic gas data on their *Low*  $N_{\text{H1}}$  mask. The offsets we found for *Planck* data are also compatible with the values derived on the same sky area by Planck Collaboration VIII (2014). The offsets derived for SPIRE data are instead negative, since the maps by construction have their median level set to zero: fields with larger emission (V1 and V2 at 250  $\mu\text{m}$ ) have a median level biased to more positive values, and the offset is more negative. As a crosscheck, we

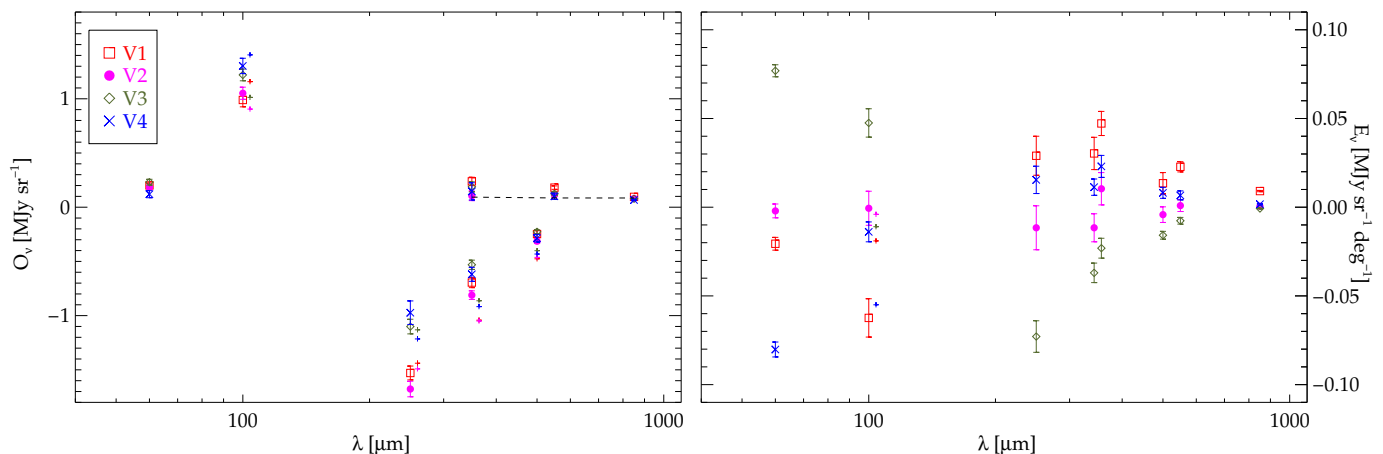


**Fig. A.1.** Left panel: offsets  $O_v$ . With crosses we show also: estimates at  $100\ \mu\text{m}$  obtained summing the offset with LAB data and the residual zodiacal light contamination in IRIS maps as derived by Planck Collaboration XI (2014); estimates for SPIRE data using the SPIRE/HFI offsets from the `zeroPointCorrection` procedure in HIPE. The dashed line shows the offset derived by the *Planck* team on zodi-corrected maps (Planck Collaboration VIII 2014). Right panel: fitted gradient in ecliptic latitude  $E_v$ . Crosses show the gradient as derived from the correction described in Planck Collaboration XI (2014). To avoid cluttering, we have slightly displaced some symbols from their exact wavelength.

also derived the offset between SPIRE and *Planck*-HFI maps using the `zeroPointCorrection` task within HIPE. The *Planck* maps used by the task have been corrected so that they also include the emission from the CIB. Thus our offset can be compared with the difference between the CIB estimate used by the *Planck* team (Planck Collaboration VIII 2014) and the HIPE offset. These values (shown as crosses at  $250$ ,  $350$  and  $500\ \mu\text{m}$  in the left panel of Fig. A.1) are compatible with those derived here at  $250\ \mu\text{m}$  (the HIPE offset resulting from a spectrum extrapolation) but show some differences at the longer wavelengths. A possible explanation might be in the uncertainties in the zero-level determination or in the spectral baseline subtraction of H1 maps, that might result in different correlations between dust emission and gas and between two dust emission channels, as noted also by Planck Collaboration VIII (2014). For the same reason, intensity levels estimated using Eq. 1 in two adjacent HeViCS fields might not overlap. However, in all cases these residual offsets are  $\leq 1\sigma$ .

The right panel of Fig. A.1 shows the fitted ecliptic latitude gradient,  $E_v$ . In half of the fits (see Table 1), the derived  $E_v$  is found to be insignificant ( $< 3\sigma$ ). When measured at  $> 3\sigma$ , it is generally consistent between SPIRE and HFI bands (i.e. always positive for fields V1 and V4, always negative for V3). However, we found it to be present also in HFI maps, which were already corrected for zodiacal light; and the V1 field has a larger gradient than V2 (where it is almost always consistent with zero), despite their common extent in ecliptic latitude. Either our naïve choice for the gradient is not able to capture the complexity of a full zodiacal light model (see Planck Collaboration XIV 2014, for the modelling of Zodiacal light in HFI maps) or it could possibly hide, as we discussed for  $O_v$ , spatial gradients due to uncertainties in the H1 spectra baseline subtraction. Gradients are also found for the IRIS data: at  $100\ \mu\text{m}$ , gradients are found to be of the same order of what can be derived from the zodiacal light subtraction of Planck Collaboration XI (2014) (crosses in the right panel of Fig. A.1). However, the largest (negative) gradient derived here is for field V1, while using the Planck Collaboration XI (2014) correction it is for field V4. Whatever is the true nature of  $E_v$ , we nevertheless retained the term in the fit because we found that it greatly reduced the scatter in the determination of the dust emissivities associated with

the IVC component, without modifying significantly the results for the LVC component.

## Appendix B: Implications for the estimate of dust mass in external galaxies

The absorption cross-section of high latitude MW dust is typically used as a proxy for the properties of dust in external galaxies. We evaluate here the impact of the new MW LVC cross-section found in *Planck* papers and in the current one, when these are used to derive the dust masses.

Bianchi (2013) argued that, under the common assumption that the FIR SED is due to dust heated by an average ISRF (Draine et al. 2007; Dale et al. 2012), fits using a single temperature MBB (essentially, using a single dust grain of average absorption cross section) do not perform much worse than fits using more realistic dust models (with a distribution of grain sizes of different materials). Assuming the same dust-to-gas mass ratio ( $\sim 0.01$ ) as derived for the Compiègne et al. (2011) dust model, and adopting their correction to account for hydrogen atoms in the ionised and molecular gas (increasing the hydrogen column density by 23%), we can derive from the current data an average dust absorption cross section per unit of mass  $\kappa_{\text{abs}}(250\mu\text{m}) = 2.2 \pm 0.6\ \text{cm}^2\ \text{g}^{-1}$  (with  $\beta = 1.5$ ). On the same sample of galaxies used in Bianchi (2013), the dust mass derived using this cross section would be on average a factor 1.55 larger than that obtained using the average properties of the FIRAS-constrained Compiègne et al. (2011) dust model, with  $\kappa_{\text{abs}}(250\mu\text{m}) = 5.1\ \text{cm}^2\ \text{g}^{-1}$  ( $\beta = 1.91$ ). In several papers of the HeViCS series we instead used  $\kappa_{\text{abs}}(350\mu\text{m}) = 1.92\ \text{cm}^2\ \text{g}^{-1}$  ( $\beta = 2$ ). Accidentally<sup>6</sup>, the dust masses obtained with this value are very close to those obtained with the new absorption cross-

<sup>6</sup> The average cross section used in most HeViCS papers (see, e.g., Smith et al. 2010; Magrini et al. 2011; Davies et al. 2012; Auld et al. 2013) was taken from the MW dust model of Draine (2003). Even though the model was constrained on the FIRAS spectrum, its emission under the LISRF heating was lower than the (corrected) DHGL SED of Compiègne et al. (2011). Bianchi (2013) maintained that this could be due to a different correction for the contribution of ionised (and molecular) gas to the hydrogen column density. Inconsistencies between *Planck* observations and the Draine (2003) mod-

section, being on average lower by 5%. Because of the lower spectral index of the new cross section, the fitted temperature would be larger, the average for the sample being  $\sim 25\text{K}$ , instead of  $\sim 21$  and  $22\text{K}$  obtained with the Compiègne et al. (2011) model spectral index and the  $\beta = 2$  HeViCS choice, respectively.

Clark et al. (2016) estimated the dust absorption cross section from integrated FIR/submm SEDs and properties for 22 galaxies in the Herschel Reference Survey (HRS; Boselli et al. 2010b). They used the mass of metals as a proxy of the dust mass and assumed a power law for the cross-section spectrum, following the method by James et al. (2002). If their analysis is repeated using  $\beta = 1.5$ , as suggested by this work, it is found that  $\kappa_{\text{abs}}(250\mu\text{m}) = 1.02_{-0.49}^{+1.09} \text{cm}^2 \text{g}^{-1}$ . The average value is lower than the estimates based on DHGL emission by a factor two, and thus the dust masses would be higher by the same factor. The discrepancy might suggest that dust in the DHGL medium has different average properties than the bulk of the dust mass in a galaxy. If this is true, dust masses might be better estimated from global SEDs using the cross sections from Clark et al. (2016); yet, the DHGL value is still within the large scatter of their estimates, which might point to galaxy-to-galaxy variations of the average dust properties.

Finally, a value  $\beta \approx 1.5$  is compatible with the SPIRE colors of the HRS galaxies (Boselli et al. 2010a, 2012). The trend in SPIRE colors could however be produced by subtle effects, such as deviations from a pure power-law in a restricted wavelength range, or by the mixing of the dust temperatures for grains of different material and size (Hunt et al. 2015). This reminds us that the result of the present work might just be an apparent  $\beta$  value providing a good description of the emissivity SED, but hiding the complexity of the dust grain mixture producing it.

### Appendix C: Data, models and residuals

Fig. C.1 to C.7 show the observed dust emission, the dust emission modelled from the H I observations, and the residuals in the IRAS 60 and  $100\mu\text{m}$  bands, the SPIRE and HFI  $350\mu\text{m}$  bands, the SPIRE  $500\mu\text{m}$  band and the HFI  $550\mu\text{m}$  band, and the HFI  $850\mu\text{m}$  band, respectively. Images follow the same criteria used to present the results for the SPIRE  $250\mu\text{m}$  band in Fig. 8.

---

els were also noted by Planck Collaboration Int. XVII (2014) and Planck Collaboration Int. XXIX (2016).

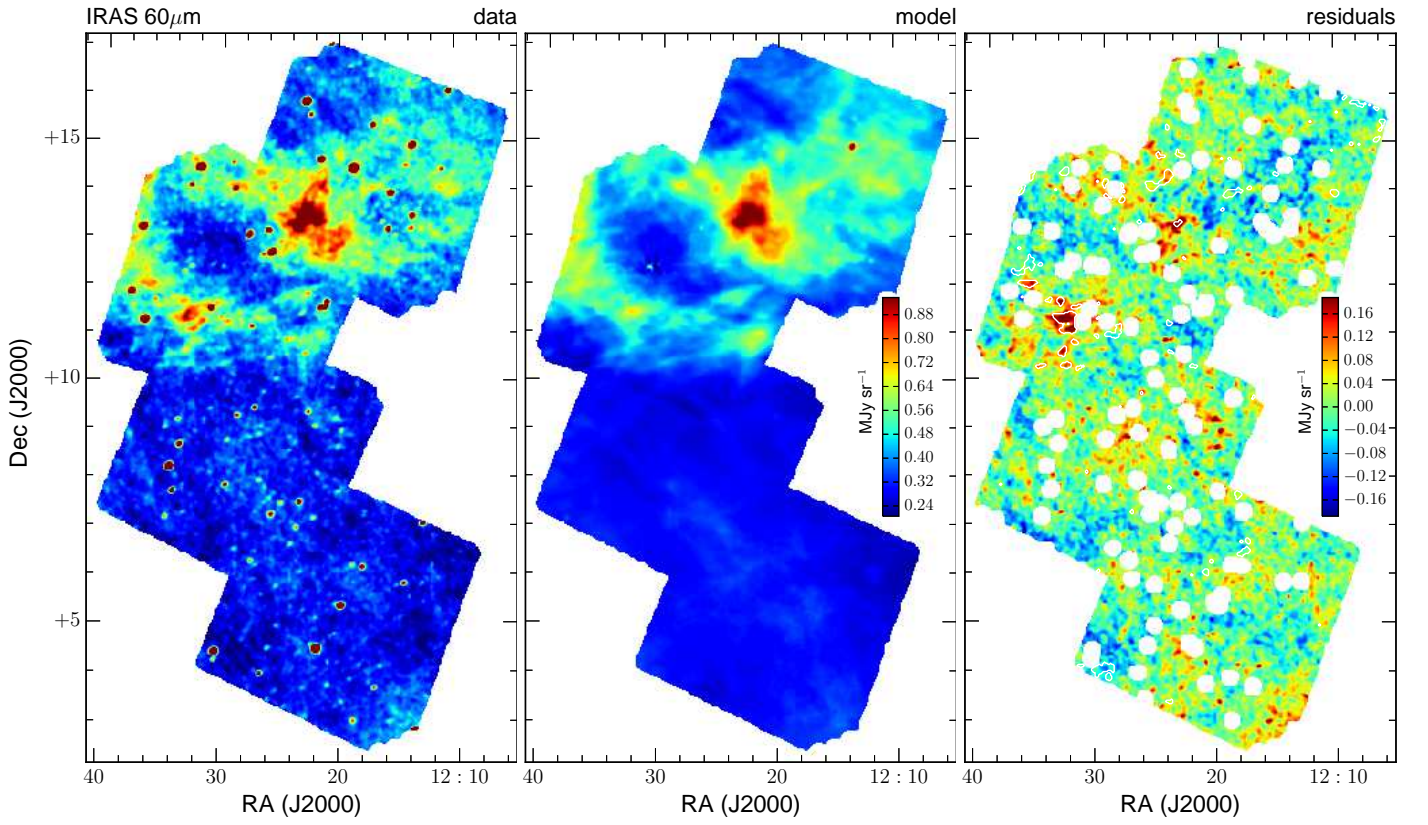


**Fig. C.1.** Same as Fig. 8, but for the IRAS 60 $\mu$ m band

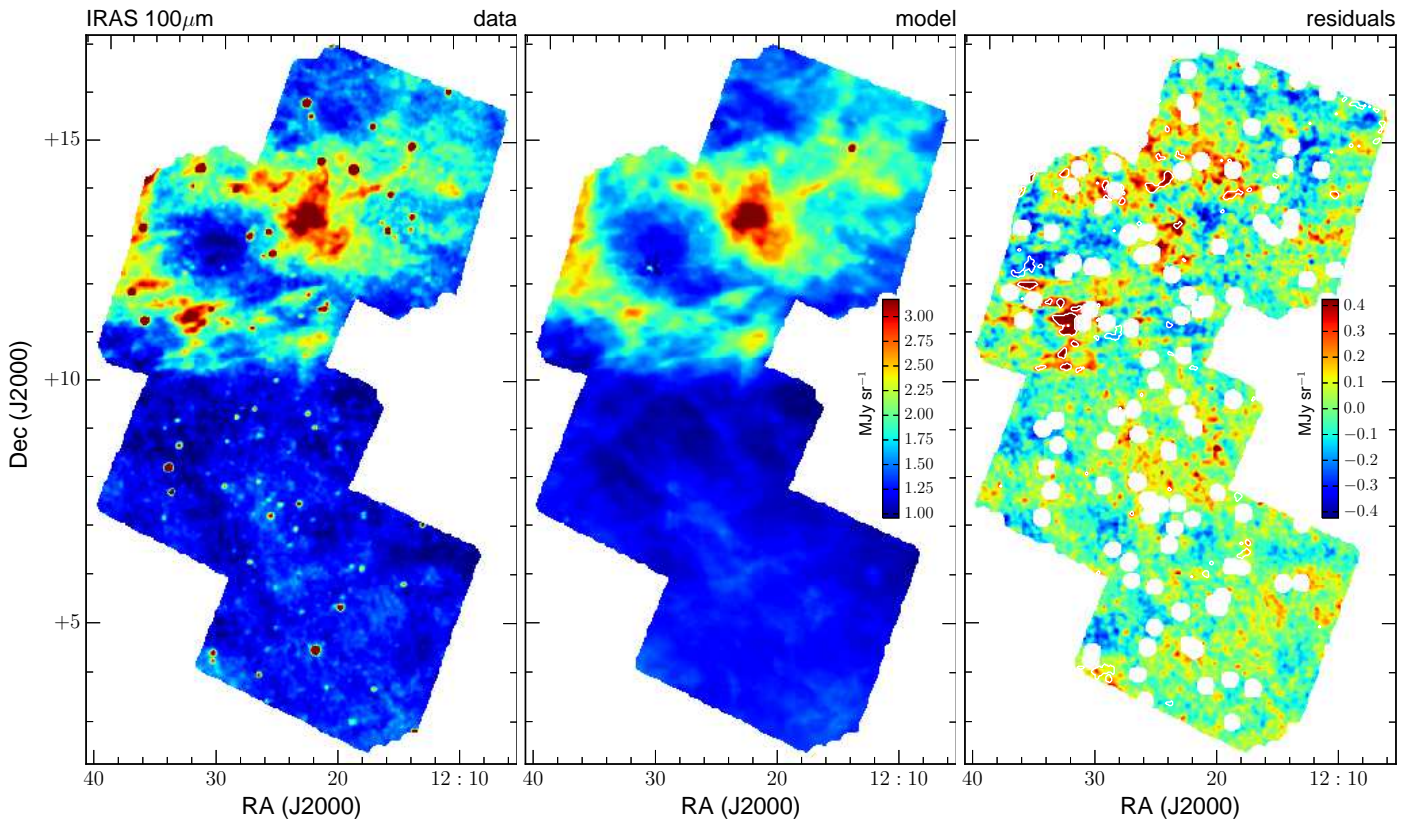


**Fig. C.2.** Same as Fig. 8, but for the IRAS 100 $\mu$ m band

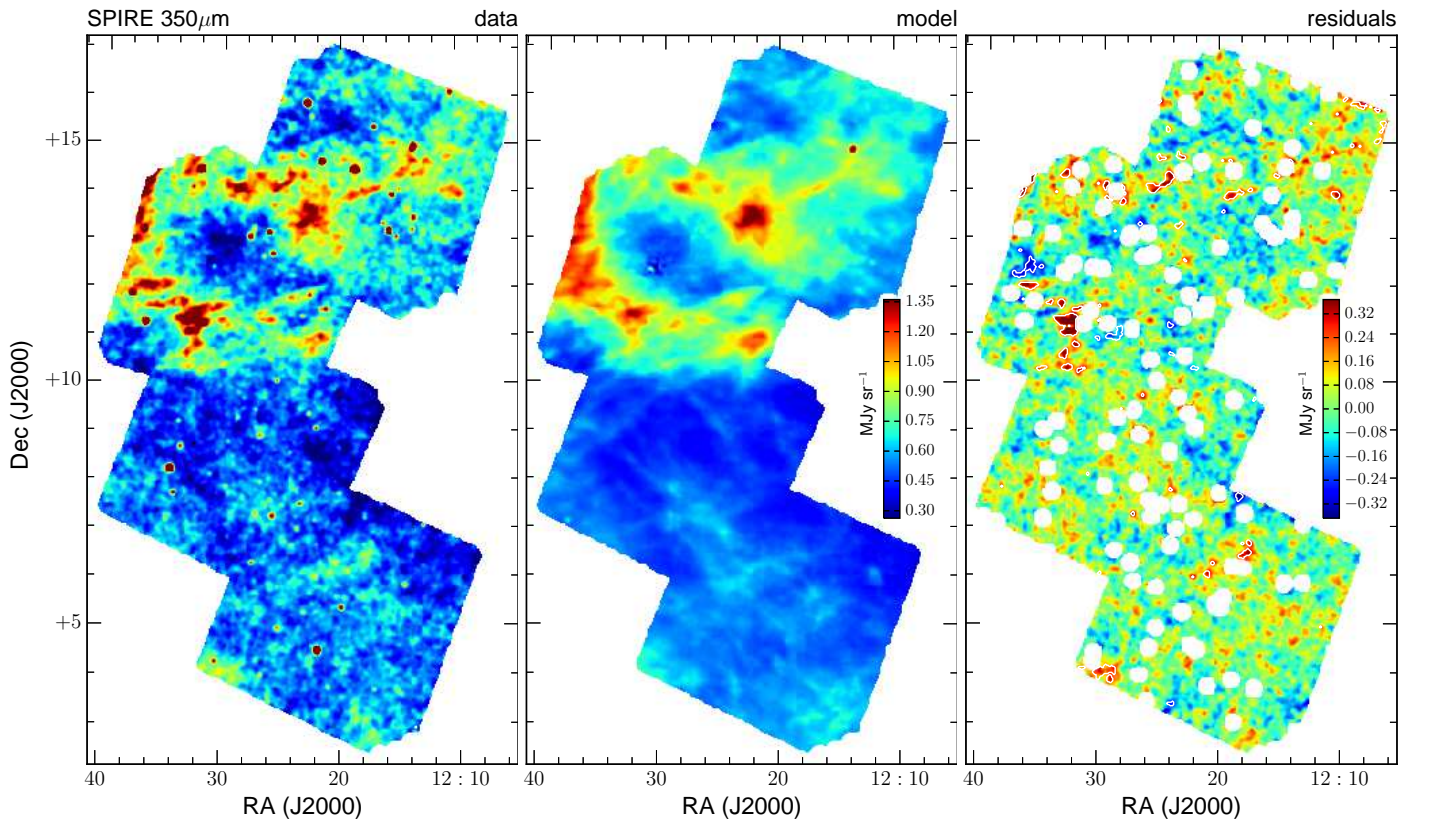


**Fig. C.3.** Same as Fig. 8, but for the SPIRE 350 $\mu$ m band

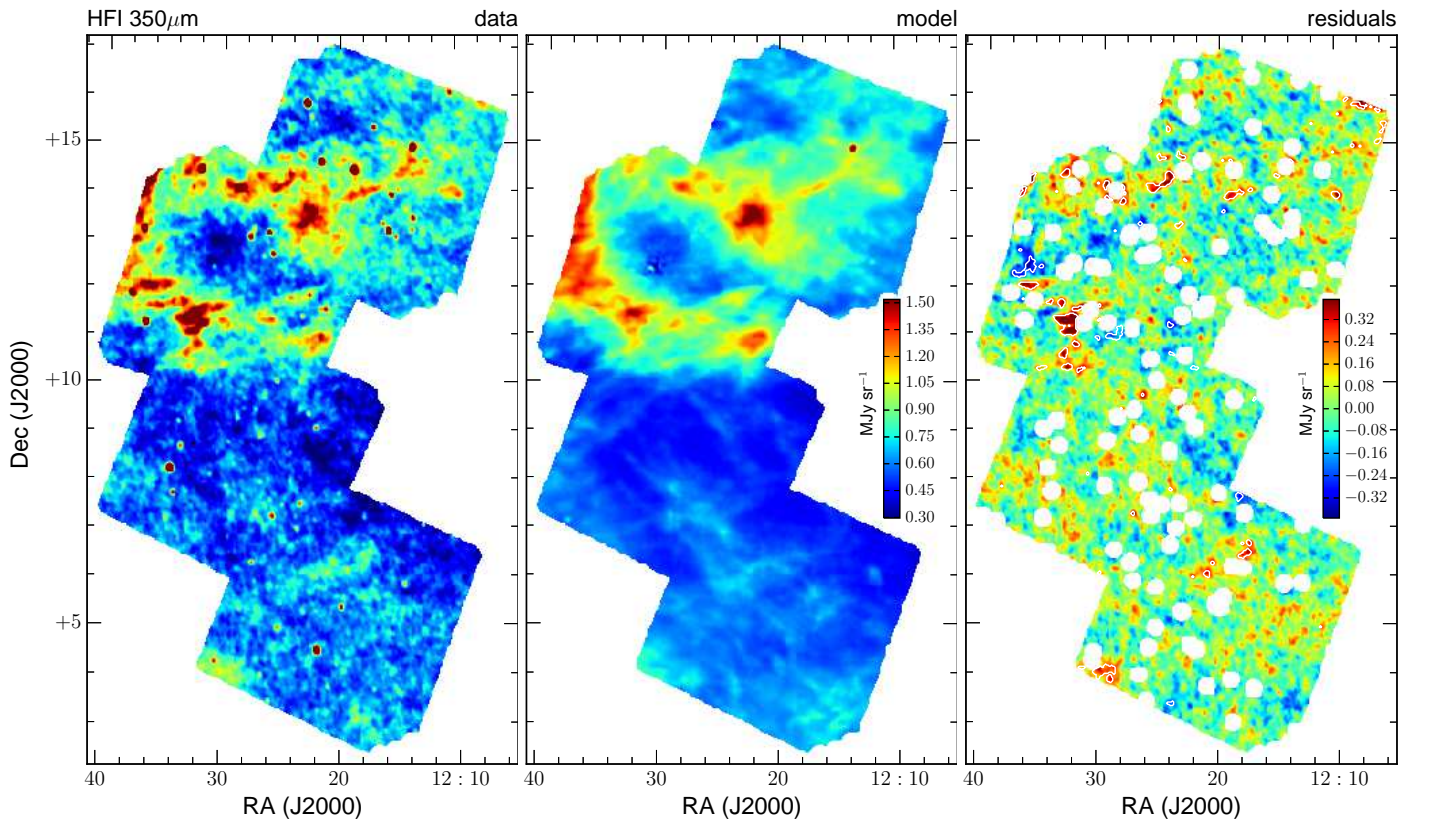


**Fig. C.4.** Same as Fig. 8, but for the HFI 350 $\mu$ m band

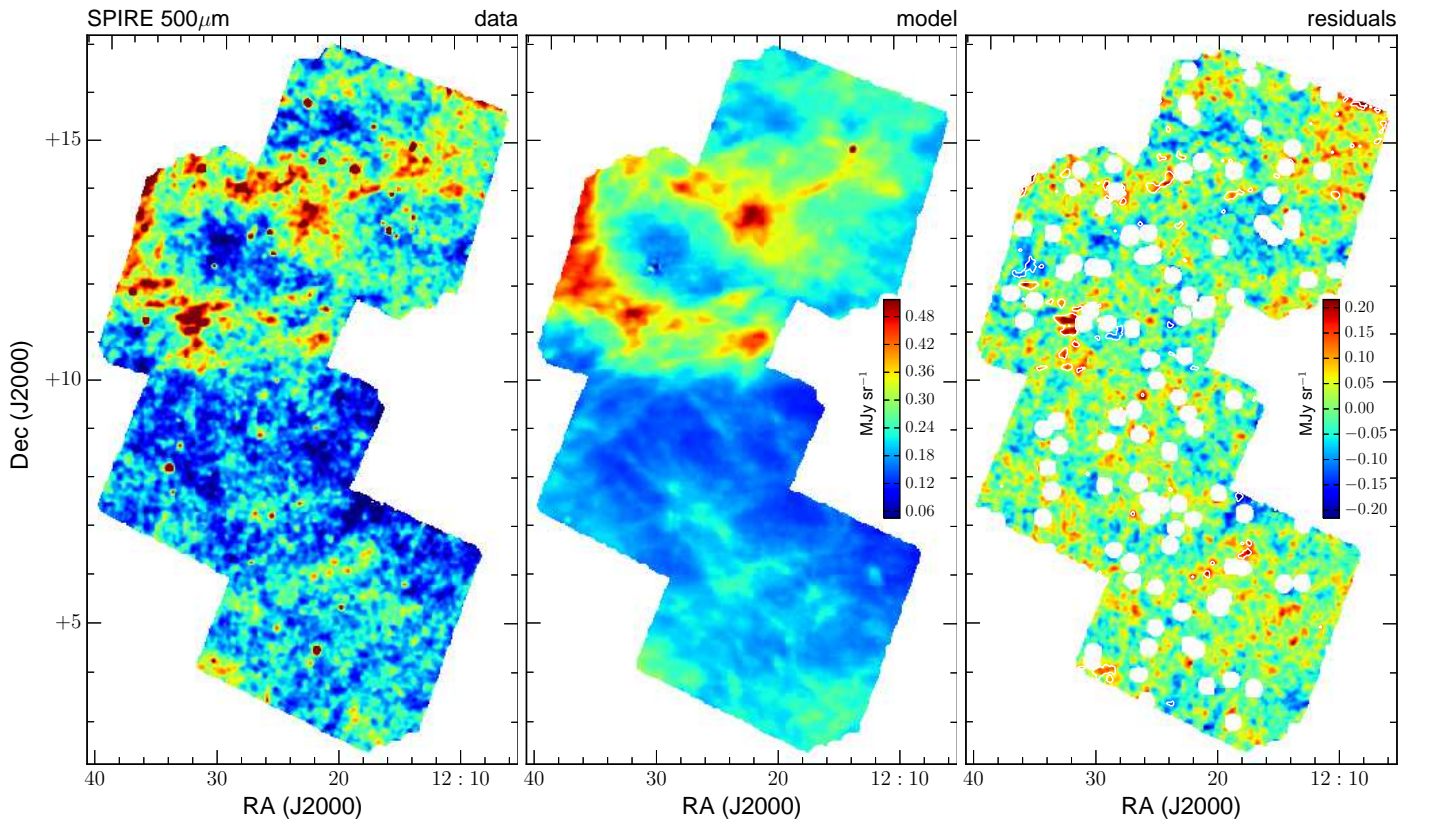


**Fig. C.5.** Same as Fig. 8, but for the SPIRE 500 $\mu\text{m}$  band

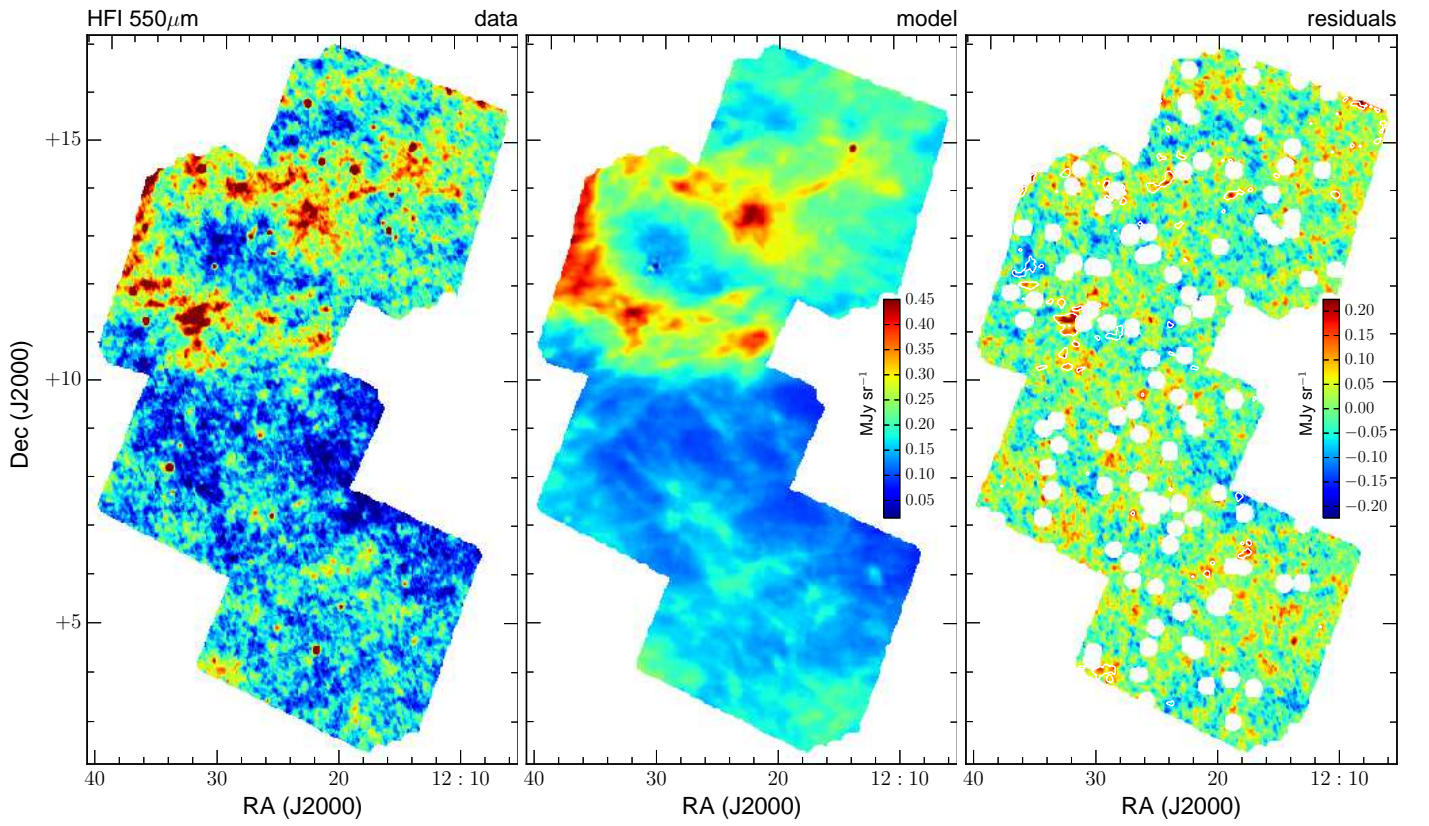


**Fig. C.6.** Same as Fig. 8, but for the HFI 550 $\mu\text{m}$  band



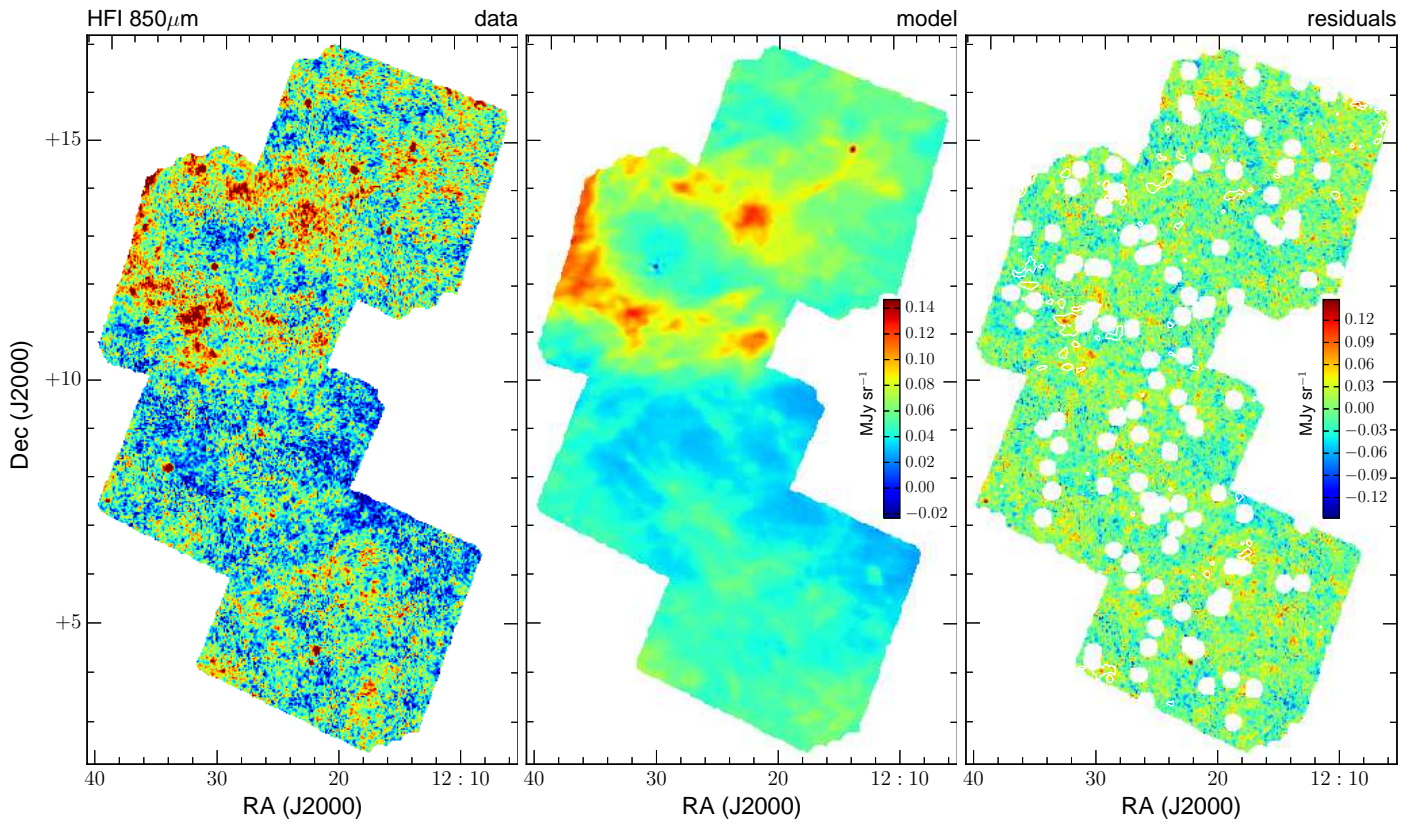


**Fig. C.7.** Same as Fig. 8, but for the HFI 850 $\mu$ m band